Progress in subgrid-scale transport modelling for continuous hybrid non-zonal RANS/LES simulations

Bruno Chaouat[*]
ONERA , 92322 Châtillon, France

Roland Schiestel[**]
IRPHE, Château-Gombert, 13384 Marseille, France

Abstract

The partially integrated transport modelling (PITM) method can be viewed as a continuous approach for hybrid RANS/LES modelling allowing seamless coupling between the RANS and the LES regions. The subgrid turbulence quantities are thus calculated from spectral equations depending on the varying spectral cutoff location [42, 8]. The PITM method can be applied to almost all statistical models to derive its hybrid LES counterpart. In the present work, the PITM version based on the transport equations for the turbulent Reynolds stresses together with the dissipation transport rate equation is now developed in a general formulation based on a new accurate energy spectrum function $E(\kappa)$ valid in both large and small eddy ranges that allows to calibrate more precisely the $c_{sgs\epsilon_2}$ function involved in the subgrid dissipation rate ϵ_{sgs} transport equation. The model is also proposed here in an extended form which remains valid in low Reynolds number turbulent flows. This is achieved by considering a characteristic turbulence length scale based on the total turbulent energy and the total dissipation rate taking into account the subgrid and resolved parts of the dissipation rate. These improvements allow to consider a large range of flows including various free flows as well as bounded flows. The present model is first tested on the decay of homogeneous isotropic turbulence by referring to the well known experiment of Comte-Bellot and Corrsin. Then, initial perturbed spectra $E(\kappa)$ with a peak or a defect of energy are considered for analysing the model capabilities in strong non-equilibrium flow situations. The second test case is the classical fully turbulent channel flow that allows to assess the performance of the model in non homogeneous flows characterised by important anisotropy effects. Different simulations are performed on coarse and refined meshes for checking the grid independence of solutions as well as the consistency of the subgrid-scale model when the filter width is changed. A special attention is devoted to the sharing out of the energy between the subgrid-scales and the resolved scales. Both the mean velocity and the turbulent stress computations are compared with data from direct numerical simulations.

---

[*] Senior Scientist, Department of Computational Fluid Dynamics. E-mail address: Bruno.Chaouat@onera.fr

[**] Senior Scientist at CNRS.

1 Introduction

Mathematical turbulence modelling methods such as Reynolds Averaged Navier-Stokes (RANS) methods or Large Eddy Simulations (LES) methods have made significant progress in the past decade for predicting aerodynamic flows and a huge variety of methods has been proposed [40]. Generally, advanced RANS models such as new generation Reynolds Stress Models (RSM) or Algebraic Reynolds Stress Models (ARSM) [26, 48] appear to be well suited for tackling engineering flows and for instance flows encountered in space propulsion [5, 7] and aeronautical applications involving strong effects of streamline curvature [24], flow separation in airfoil problems [37, 6, 27], rotating flows [4], adverse pressure gradient boundary layers whereas LES methods using subgrid scale models such as for instance the dynamic model [19] or the structure model [32] are successfully applied for simulating academic flows with emphasis on fundamental aspects and structural aspects, together with statistical post-analysis based on two-point correlations and spectral properties. The current trends in turbulence modelling using these approaches, have been recently reviewed by Gatski et al. for turbulent aerodynamic flows [17] and by Lesieur and Métais [28] for large eddy simulations, pointing out their respective advantages and drawbacks. Although these methods are very useful, each of them has its own specific field of application. It appears for instance that statistical RANS models are not well suited for studying unsteady flows when they are subjected to a large range of frequencies that can interact with the turbulence time scales. On the other hand, large eddy simulations are not always accurate when they are performed on coarse grids since an appreciable part of the subgrid-scale turbulence needs to be modelled and this is generally made using a simple closure only valid for fine grained turbulence, and rarely by using a transport equation. This situation occurs when the cutoff wavenumber may be located before the inertial range. Moreover, large eddy simulations require very large computing time and this is not always affordable in industrial applications, even with the rapid increase in computer speed [31]. For these reasons, hybrid RANS/LES zonal methods, capable of reproducing a RANS-type behaviour in the vicinity of a solid boundary and an LES-type behaviour far away from the wall boundary have been developed in the last decade [45]. Among these methods, the detached eddy simulation (DES) developed by Spalart and Allmaras [46], where the model is switching from a RANS behaviour to an LES behaviour depending on a criteria based on the turbulent length-scale is the most used model. It is often applied in aeronautical industries. Some other RANS/LES zonal methods have also been developed in this framework but they rely on two different models, a RANS model and a subgrid-scale model, which are applied in different domains separated by an interface [22, 49, 50]. These zonal methods allow an appreciable saving of CPU time because only a particular region of the flow has to be solved using a refined mesh to describe the turbulence field. Noticeably, the main shortcoming of these methods lies in the connection interface between the RANS and LES regions. The interface is empirically set inside the computational domain and the turbulence closure changes from one model to another one without continuity when crossing the interface. These methods often require an internal forcing produced by artificial instantaneous random fluctuations for restoring continuity at the crossflow between these domains. These practices may be necessary in order to get the correct velocity and stress profiles in the boundary layer [13].

To get rid of interface problems, the partially integrated transport modelling (PITM) approach for the subgrid turbulence quantities has been developed by Schiestel and Dejoan for the energy subfilter model [42] and by Chaouat and Schiestel for the stress subfilter model [8]. It can be viewed as a continuous non-zonal hybrid RANS/LES method with seamless coupling. It bridges two different levels of description in a consistent way based on the spectral theoretical PITM methodology [23, 9] and then allows to transpose the advantages of advanced RANS modelling such as Reynolds stress models to LES simulations. Thus, it gains major interest on the fundamental point of view because it allows some unifying formalism that conciliates RANS and LES approaches. In particular, the subfilter model based on the transport equations for the subfilter stresses and the dissipation rate appears to be nicely appropriate for simulating unsteady flow regimes with a high resolution of the turbulence anisotropy [8, 9]. In regard with academic LES simulations which require that the spectral cutoff is located within the inertial range, the PITM models allow to perform flow simulations on relatively coarse grids since the cutoff wavenumber can be located almost anywhere inside the spectrum. In that case, an important part of the subgrid-scale energy is modelled using the second order closure method whereas the large scales are resolved by the numerical scheme. Then, the total stresses are computed as the sum of the subgrid and large scale parts. In the present approach, the dissipation rate is computed from the modelled transport equation for the spectral flux. The theory shows that the coefficients are no longer constants but must be a function of the cutoff wavenumber. This constitutes the main feature of the PITM method. As a result, the PITM method appears well suited for simulating non-equilibrium flows with departures from the standard Kolmogorov law.

From a physical point of view, the PITM approach finds its basic foundation in the spectral space by considering the Fourier transform of the two-point fluctuating velocity correlation equations in homogeneous turbulence. The extension to non-homogeneous turbulence can be developed easily within the approximate framework of the tangent homogeneous space [9]. Moreover, the transport equation of the spectral velocity correlation tensor in wave vector space allows to characterise each physical process such as production, redistribution, transfer, diffusion and dissipation acting in spectral zones. The dissipation rate is then interpreted as a spectral flux of energy transferred from large eddies to small eddies by the inertial cascade down to the last slice of the spectrum. This spectral equation is the cornerstone of the PITM method.

The present paper presents the main features and the basic hypotheses in the PITM method that allows transposition of turbulence models from RANS to LES. New developments that extend the previous energy and stress subfilter models [8] to a larger range of flows are then presented and discussed in details. The model is mainly dedicated to the study of nonstandard spectral distribution with departures from the standard Kolmogorov distribution and the improvements presented here allow to consider low Reynolds number flows. The subfilter models will be developed in a more general formulation based on a new energy spectrum function $E(\kappa)$ valid throughout the entire spectrum. Consequently, a more accurate calibration of the $c_{sgs\epsilon_2}$ function coefficient involved in the transport equation for the subgrid dissipation rate [8] is possible. The model will be also proposed in an extended approach that can be applied to a larger range of flows considering that the turbulence length scale L_e is built on the total turbulent energy k and the total dissipation rate ϵ, including both the subgrid scale dissipation rate ϵ_{sgs} and the resolved scale dissipation rate rate $\epsilon^<$, leading thus to the relation $L_e = k^{3/2}/(\langle\epsilon_{sgs}\rangle + \langle\epsilon^<\rangle)$. Thus, the model can be developed in a low Reynolds number version capable of reproducing the dissipative effects in the resolved range of eddies. The model is first tested on the decay of homogeneous isotropic turbulence referring to the experiment of Comte-Bellot and Corrsin. Then, initial perturbed spectra $E(\kappa)$ with a peak or a defect of energy are considered in order to analyse the capabilities of the model in non-equilibrium flow situations. The second test case is the well known fully developed turbulent channel flow that allows to assess the performance of the model in non homogeneous flows, and especially, its capability to reproduce the flow anisotropy, even for LES simulations performed on coarse grids. The simulations are performed on two different meshes for checking the grid independence of the solutions as well as the consistency of the subgrid-scale model when the filter width is changed.

2 PITM approach to subgrid-scale turbulence models

2.1 The filtering and averaging processes

Reynolds averaged Navier-Stokes method assumes that each variable ϕ can be decomposed into an ensemble average part $\langle\phi\rangle$ and a fluctuating part that embodies all the turbulent scales ϕ' such as $\phi = \langle\phi\rangle + \phi'$. So, the turbulence closure then consists in modelling the energy spectrum as a whole. In practice, the Reynolds averaging is often obtained by using time averaging over a sufficiently long period in comparison with the turbulent time scale. On the contrary, the large eddy simulation method consists in modelling only the small scales of turbulence which are more universal whereas the large scales are resolved explicitly by the numerical scheme. In that situation, the spectrum is thus partitioned into two zones delimited by the cutoff wavenumber κ_c, usually defined from the grid size Δ, $\kappa_c = \pi/\Delta$. In the present PITM approach, another wavenumber κ_d located at the far end of the inertial range of the spectrum is also introduced, assuming that the energy pertaining to higher wavenumbers is entirely negligible. The use of the dissipative wavenumber κ_d comes from the multiple scale modelling [38] in which this spectral splitting avoids to consider infinite limits and molecular viscosity effects in the far end of the spectrum. In this framework, the instantaneous variable ϕ is then decomposed into a filtered part $\bar{\phi}$ and a small scale modelled part $\phi^>$ such that $\phi = \bar{\phi} + \phi^>$. The instantaneous fluctuation ϕ' contains in fact the large scale fluctuating part $\phi^<$ and the small scale fluctuating part $\phi^>$ such that $\phi' = \phi^< + \phi^>$. The instantaneous variable ϕ can then be rewritten like the sum of a mean statistical part $\langle\phi\rangle$, a large scale fluctuating part $\phi^<$ and a small scale fluctuating part $\phi^>$ as follows $\phi = \langle\phi\rangle + \phi^< + \phi^>$. The first two terms correspond to the filtered velocity $\bar{\phi} = \langle\phi\rangle + \phi^<$ implying that the large scale fluctuating part is simply the difference between the filtered and the statistical quantities, $\phi^< = \bar{\phi} - \langle\phi\rangle$. In fact, the large scale fluctuations (resolved scales) and the fine scales fluctuations(modelled scales) can be naturally defined from the physical meaning of the Fourier transform of the fluctuating quantities ϕ' using the cutoff wavenumber κ_c as the lower bound of the integration interval. Indeed, if working in spectral space, the large scale $\phi^<$ and the fine scale $\phi^>$ are then defined from the Fourier transforms :

$$\phi^< = \int_{|\kappa|\leq\kappa_c} \widehat{\phi}'(\boldsymbol{X}, \boldsymbol{\kappa}) \exp\left(j\boldsymbol{\kappa}\boldsymbol{\xi}\right)\, d\boldsymbol{\kappa} \tag{1}$$

$$\phi^{>} = \int_{|\kappa| \geq \kappa_c} \widehat{\phi'}(\boldsymbol{X}, \boldsymbol{\kappa}) \exp\left(j \boldsymbol{\kappa} \boldsymbol{\xi}\right) \, d\boldsymbol{\kappa} \tag{2}$$

At this step, the question now is to show the connection that may exist between the filtered and statistical mean value: does a filtered quantity goes to the statistical mean when the filter width goes to infinity? This is obvious in homogeneous turbulence, considering the previous formula. But for non-homogeneous turbulence, which is indeed the usual case, it is necessary then to consider the concept of tangent homogeneous space at a point of a non-homogeneous flow field assuming Taylor series expansion in space for the mean velocity field [9, 41]. Indeed, this concept ensures that the filtered field goes to the statistical mean field when the filter width goes to infinity ($\Delta \to \infty$, $\kappa_c \to 0$ and $\overline{\phi} \to \langle \phi \rangle$). In particular, when the cutoff vanishes, the full integration in the tangent homogeneous space exactly corresponds to the statistical mean, that guarantees exact compatibility with RANS equations [9]. We insist on the fact that integration is performed in the tangent homogeneous space and not in the real space itself. Therefore, in this approach, the particular filter defined by the spectral truncations (1) and (2) can be used to derive transport equation that have the same form as in statistical multiscale models because the large scale and small scale fluctuations are uncorrelated $\langle \varphi^{>} \psi^{<} \rangle = 0$.

2.2 The governing equations

By applying the filter on the instantaneous momentum equation one then derives the filtered momentum equation

$$\frac{\partial \bar{u}_i}{\partial t} + \frac{\partial}{\partial x_j}\left(\bar{u}_i \bar{u}_j\right) = -\frac{1}{\rho}\frac{\partial \bar{p}}{\partial x_i} + \nu \frac{\partial^2 \bar{u}_i}{\partial x_j \partial x_j} - \frac{\partial \tau(u_i, u_j)}{\partial x_j} \tag{3}$$

in which the subgrid-scale tensor is defined by the mathematical function

$$(\tau_{ij})_{sgs} = \tau(u_i, u_j) = \overline{u_i u_j} - \bar{u}_i \bar{u}_j \tag{4}$$

To make clear the bridge between the RANS and LES approaches, we also recall the statistical averaged momentum equation that reads

$$\frac{\partial \langle u_i \rangle}{\partial t} + \frac{\partial}{\partial x_j}\big(\langle u_i \rangle \langle u_j \rangle \big) = -\frac{1}{\rho}\frac{\partial \langle p \rangle}{\partial x_i} + \nu \frac{\partial^2 \langle u_i \rangle}{\partial x_j \partial x_j} - \frac{\partial \tau_{ij}}{\partial x_j} \tag{5}$$

where the Reynolds stress in the statistical sense τ_{ij} includes the small scale and large scale contributions

$$\tau_{ij} = \langle u_i u_j \rangle - \langle u_i \rangle \langle u_j \rangle = \langle u'_i u'_j \rangle = \left\langle u_i^{<} u_j^{<} \right\rangle + \left\langle u_i^{>} u_j^{>} \right\rangle \tag{6}$$

Because of the nice property of the spectral filter defined by the Fourier transform, one can remark that the statistical average of the subgrid-scale stress is then simply the average of the small scale fluctuating velocities $\langle (\tau_{ij})_{sgs} \rangle = \langle u_i^{>} u_i^{>} \rangle$. Similarly, the resolved scale tensor can be defined by the relation

$$(\tau_{ij})_{les} = \bar{u}_i \bar{u}_j - \langle u_i \rangle \langle u_j \rangle \tag{7}$$

with the property $\langle(\tau_{ij})_{les}\rangle = \left\langle u_i^< u_j^< \right\rangle$. So that, the Reynolds stress tensor τ_{ij} can be computed by the sum of the statistical average of subgrid and resolved stresses

$$\tau_{ij} = \langle(\tau_{ij})_{sgs}\rangle + \langle(\tau_{ij})_{les}\rangle \tag{8}$$

and the statistical turbulent energy is obtained as the half-trace of equation (8)

$$k = \langle k_{sgs}\rangle + \langle k_{les}\rangle \tag{9}$$

Closure of equation (3) is then necessary for the subgrid-scale tensor. In the present approach, this is achieved by means of a transport equation in order to get a more general closure allowing a more realistic and precise description of the flow anisotropy than eddy viscosity models and also to get a better account of history and non-equilibrium effects. This is particularly important when the cutoff goes into the non-universal range of the spectrum located before the inertial range. As usually made in LES simulations, the statistical average of the resolved stress $\langle(\tau_{ij})_{les}\rangle$ which corresponds to the correlation of the large scale fluctuating velocities $\left\langle u_i^< u_j^< \right\rangle$ appearing in equation (6) is computed by a numerical procedure using the relation

$$\langle(\tau_{ij})_{les}\rangle = \left\langle u_i^< u_j^< \right\rangle = \langle \bar{u}_i \bar{u}_j \rangle - \langle \bar{u}_i \rangle \langle \bar{u}_j \rangle \tag{10}$$

2.3 Exact transport equation for the subgrid-scale stress

The first step of the present approach consists in writing the exact transport equation of the subgrid-scale stress $(\tau_{ij})_{sgs}$. Following the work of Germano [18], it appears that the transport equation for the subgrid-scale tensor takes a generic form if written in terms of central moments

$$\begin{aligned}\frac{\partial \tau(u_i,u_j)}{\partial t} + \frac{\partial}{\partial x_k}\left[\tau(u_i,u_j)\bar{u}_k\right] = -\tau(u_i,u_k)\frac{\partial \bar{u}_j}{\partial x_k} - \tau(u_j,u_k)\frac{\partial \bar{u}_i}{\partial x_k} + \tau\left(p, \frac{\partial u_i}{\partial x_j} + \frac{\partial u_j}{\partial x_i}\right) \\ -\frac{1}{\rho}\frac{\partial \tau(p,u_i)}{\partial x_j} - \frac{1}{\rho}\frac{\partial \tau(p,u_j)}{\partial x_i} - \frac{\partial \tau(u_i,u_j,u_k)}{\partial x_k} + \nu\frac{\partial^2 \tau(u_i,u_j)}{\partial x_k \partial x_k} - 2\nu\tau\left(\frac{\partial u_i}{\partial x_k}, \frac{\partial u_j}{\partial x_k}\right)\end{aligned} \tag{11}$$

where in this equation, we have extended the basic definition (4) to general functions of two variables

$$\tau(f,g) = \overline{fg} - \bar{f}\bar{g} \tag{12}$$

and three variables

$$\tau(f,g,h) = \overline{fgh} - \bar{f}\tau(g,h) - \bar{g}\tau(h,f) - \bar{h}\tau(f,g) - \bar{f}\bar{g}\bar{h} \tag{13}$$

applicable for any turbulent quantities f, g, h. Then, the resulting equation for the subgrid stress can be rearranged in a simple form by identifying each turbulence interaction as follows:

$$\frac{\partial \tau(u_i,u_j)}{\partial t} + \frac{\partial}{\partial x_k}\left[\tau(u_i,u_j)\bar{u}_k\right] = (P_{ij})_{sgs} + (\Psi_{ij})_{sgs} + (J_{ij})_{sgs} - (\epsilon_{ij})_{sgs} \tag{14}$$

In this equation, the term $(P_{ij})_{sgs}$ represents the production of turbulence due to the interaction between the subgrid-scale stress and the filtered velocity gradient

$$(P_{ij})_{sgs} = -\tau(u_i, u_k)\frac{\partial \bar{u}_j}{\partial x_k} - \tau(u_j, u_k)\frac{\partial \bar{u}_i}{\partial x_k}\,, \tag{15}$$

the term Ψ_{ij} acts to redistribute the turbulent energy among the subgrid-scale stress components, it plays a pivotal role in second order closures by taking into account the flow anisotropy and nonlocal effects of the turbulence

$$(\Psi_{ij})_{sgs} = \tau\left(\frac{p}{\rho}, \frac{\partial u_i}{\partial x_j} + \frac{\partial u_j}{\partial x_i}\right)\,, \tag{16}$$

the term J_{ij} denotes the diffusion term due to the fluctuating velocities and pressure together with the molecular diffusion

$$(J_{ij})_{sgs} = -\frac{\partial \tau(u_i, u_j, u_k)}{\partial x_k} - \frac{1}{\rho}\frac{\partial \tau(p, u_i)}{\partial x_j} - \frac{1}{\rho}\frac{\partial \tau(p, u_j)}{\partial x_i} + \nu\frac{\partial^2 \tau(u_i, u_j)}{\partial x_k \partial x_k}\,, \tag{17}$$

and finally, the turbulent viscous dissipation $(\epsilon_{ij})_{sgs}$ which is generated by the interaction between the subgrid-scale velocity gradients reads

$$(\epsilon_{ij})_{sgs} = 2\nu\,\tau\left(\frac{\partial u_i}{\partial x_k}, \frac{\partial u_j}{\partial x_k}\right)\,. \tag{18}$$

By using the material derivative operator $D/Dt = \partial/\partial t + \bar{u}_k \partial/\partial x_k$, equation (14) can be rewritten in a simple compact form as follows

$$\frac{D(\tau_{ij})_{sgs}}{Dt} = (P_{ij})_{sgs} + (\Psi_{ij})_{sgs} + (J_{ij})_{sgs} - (\epsilon_{ij})_{sgs} \tag{19}$$

whereas the equation for the subgrid energy is obtained as half the trace of equation (19)

$$\frac{Dk_{sgs}}{Dt} = P_{sgs} + J_{sgs} - \epsilon_{sgs} \tag{20}$$

where $P_{sgs} = (P_{mm})_{sgs}/2$, $J_{sgs} = (J_{mm})_{sgs}/2$, and $\epsilon_{sgs} = (\epsilon_{mm})_{sgs}/2$. From its definition, it is recalled that the redistribution term Ψ_{ij} vanishes through tensorial contraction because of the continuity equation. As it was mentioned in the preceding section, the mean statistical and filtered equations can be written in a similar form because of the nice particular property of the spectral truncation filter. For instance, the return to isotropy term in statistical modelling Ψ_{ij} is given by the well known expression

$$\Psi_{ij} = \left\langle \frac{p}{\rho}\left(\frac{\partial u_i}{\partial x_j} + \frac{\partial u_j}{\partial x_i}\right)\right\rangle - \left\langle \frac{p}{\rho}\right\rangle \left\langle \frac{\partial u_i}{\partial x_j} + \frac{\partial u_j}{\partial x_i}\right\rangle = \left\langle \frac{p'}{\rho}\left(\frac{\partial u'_i}{\partial x_j} + \frac{\partial u'_j}{\partial x_i}\right)\right\rangle \tag{21}$$

whereas the subgrid term $(\Psi_{ij})_{sgs}$ takes the corresponding expression as follows

$$(\Psi_{ij})_{sgs} = \overline{\frac{p}{\rho}\left(\frac{\partial u_i}{\partial x_j} + \frac{\partial u_j}{\partial x_i}\right)} - \frac{\overline{p}}{\rho}\overline{\left(\frac{\partial u_i}{\partial x_j} + \frac{\partial u_j}{\partial x_i}\right)} \tag{22}$$

showing clearly the formal analogy between the statistical and filtered approaches and their compatibility. As a consequence, the closure approximations used for the statistical partially averaged equations are assumed to prevail also in the case of large eddy numerical simulations. This formalism allows to derive the PITM models like the subgrid energy model developed by Schiestel and Dejoan [42] based on the transport equation (20) as well as the subgrid stress model proposed by Chaouat and Schiestel [8] based on the transport equation (19).

2.4 Modelling of the transport equation for the subgrid-scale stress

As usually made in statistical models, the next step consists in modelling each term appearing in the exact equation (11) under physical considerations. In particular, following the formalism developed for statistical modelling, the redistribution term $(\Psi_{ij})_{sgs}$ given by equation (16) or equation (22) if written in a developed form involves the subgrid-scale fluctuating pressure which is solution of the Poisson equation. When integrating this equation in space using the Green's function solution and then multiplying by the subgrid-scale strain, it is found as a result that the redistribution term is therefore decomposed into a slow part $(\Psi^1_{ij})_{sgs}$, function of the fluctuating velocities, and a rapid part $(\Psi^2_{ij})_{sgs}$, involving the filtered velocity gradients. From a physical point of view, the analogy between the RANS and LES modelling and in particular the assumption that the Rotta/rapid terms splitting and their linear relationship approximation as a function of the Reynolds/SGS stress tensor hold in the case of subfilter closure supposing highly unsteady perturbations is not straightforward. There are however several arguments to comfort this hypothesis. The analogy in the stress transport equations in RANS and LES forms is an important favourable point but this is not a sufficient point. The main important point is that in classical turbulence phenomenology the small scales (small eddies) are recognized to have also small characteristic time scale (they evolve rapidly). The concepts of energy cascade and return to isotropy which are more or less active at all scales suggest that it is reasonable to think that the mechanisms prevailing for small eddies subjected to the deformation produced by the large eddies is comparable to the action of the mean flow on the big eddies themselves. This leads to use analogous models of closure in both cases. The big eddies have large time scales and so their unsteadiness is not so high in frequency than the unsteadiness of the small eddies that have some time to "go to isotropy ". This hypothesis is so natural that it was already used in the pioneering work of Deardorff [14]. In the LES framework the hypothesis would need to be demonstrated by *a priori* testing from experiments or fine DNS. These same remarks also apply to the diffusion process. For LES simulations, these terms $(\Psi^1_{ij})_{sgs}$ and $(\Psi^2_{ij})_{sgs}$ are now modelled in the range $[\kappa_c, \kappa_d]$ where the cutoff wave number κ_c is usually computed from the grid size $\kappa_c = \pi/\Delta$ (note that this is the usual practice but the only requirement is that the filter width is larger or equal to the grid step) and κ_d is the dissipative wave number located at the end of the inertial range of the spectrum completely after the transfer zone. The slow term $(\Psi^1_{ij})_{sgs}$ which characterises the return to isotropy due to the action of turbulence on itself may depend on the spectral zone. Since the small scales return more rapidly to isotropy than the large scales which are more permanent in time before cascading into smaller scales by non-linear interactions, the slow term $(\Psi^1_{ij})_{sgs}$ must increase with the wave number κ_c in order to strengthen the return to isotropy in the range of larger wave numbers. Requiring also that usual statistical Reynolds stress models must be recovered in the limit of vanishing cutoff wave number

κ_c, the slow redistribution term is modelled as [38]

$$(\Psi^1_{ij})_{sgs} = -c_{sgs_1} \frac{\epsilon_{sgs}}{k_{sgs}} \left((\tau_{ij})_{sgs} - \frac{1}{3} (\tau_{mm})_{sgs} \delta_{ij} \right) \tag{23}$$

where c_{sgs_1} is a continuous function of the dimensionless parameter $\eta_c = \kappa_c L_e$ involving the characteristic turbulence length scale L_e. This function is empirically proposed in the following form

$$c_{sgs_1}(\eta_c) = c_1 \, \frac{1 + \alpha_{\eta 1} \, \eta_c^2}{1 + \alpha_{\eta 2} \, \eta_c^2} \tag{24}$$

In this relation, c_1 is the usual Rotta constant used in statistical modelling, and $\alpha_{\eta 1}$ and $\alpha_{\eta 2}$ are numerical coefficients satisfying the condition $\alpha_{\eta 1} > \alpha_{\eta 2}$. The function $c_{sgs_1}(\eta_c)$ satisfies the limiting condition $\lim_{\eta_c \to 0} c_{sgs_1}(\eta_c) = c_1$. The fact that the coefficient c_{sgs_1} must increase with the wave number is also justified by direct numerical simulations [35] made in homogeneous anisotropic turbulent flows for various types of strain [39]. In this study, the slow term $(\Psi^1_{ij})_{sgs}$ was calculated in the spectral space from averaging in spherical shells, and the dependence of c_{sgs_1} with respect to the wave number was obtained. The turbulence length scale $L_e = k^{3/2}/(\langle \epsilon_{sgs} \rangle + \langle \epsilon^< \rangle)$ is now built by means of the total turbulent energy obtained as the sum of the subgrid and large scale parts $k = \langle k_{sgs} \rangle + \langle k_{les} \rangle$, and the total dissipation rate $\epsilon = \langle \epsilon_{sgs} \rangle + \langle \epsilon^< \rangle$, including the dissipation in the subgrid zone ϵ_{sgs} and the resolved part of the dissipation rate defined by

$$\epsilon^< = \nu \, \overline{\frac{\partial u_i^<}{\partial x_j} \frac{\partial u_i^<}{\partial x_j}} \tag{25}$$

caused by the large-scale fluctuating velocities $u_i^< = \bar{u}_i - \langle u_i \rangle$. This contribution to dissipation may become not negligible in low Reynolds number flows. In contrast with the simplified formulation assuming linear length scale, first introduced for wall bounded flows $L = K x_n$ where K is the Von Kármán constant [8], the new definition of the parameter η_c is now given by

$$\eta_c = \kappa_c L_e = \frac{\pi \, k^{3/2}}{(\Delta_1 \Delta_2 \Delta_3)^{1/3} \, (\langle \epsilon_{sgs} \rangle + \langle \epsilon^< \rangle)} \tag{26}$$

where Δ_i is the filter width in the ith direction. Note that equation (26) needs to compute the total turbulent energy as well as the total dissipation rate by statistical averaging at each time advancement step during the simulation. In practice, their statistical value is calculated from simulation results at the previous time step. The filter width has been defined as the cubic root of the product $\Delta_1 \Delta_2 \Delta_3$ for regular grids but more elaborated formulations can be proposed for skewed grids [44]. However, this refinement has not been used in the present calculations. The second term $(\Psi^2_{ij})_{sgs}$ corresponds to the linear return to isotropy produced by the filtered velocity gradients and is therefore physically not affected by the spectral zone. In this case, the usual statistical modelling form is retained

$$(\Psi^2_{ij})_{sgs} = -c_2 \left((P_{ij})_{sgs} - \frac{1}{3} (P_{mm})_{sgs} \, \delta_{ij} \right) \tag{27}$$

although $(\Psi^2_{ij})_{sgs}$ is now a fluctuating quantity because the filtered velocity evolves rapidly in time and space. As usual, the diffusion process $(J_{ij})_{sgs}$ is modelled assuming a gradient law hypothesis that prevail for subgrid-scale modelling. The approximation is

$$(J_{ij})_{sgs} = \frac{\partial}{\partial x_k}\left(\nu\frac{\partial(\tau_{ij})_{sgs}}{\partial x_k} + c_s\frac{k_{sgs}}{\epsilon_{sgs}}(\tau_{kl})_{sgs}\frac{\partial(\tau_{ij})_{sgs}}{\partial x_l}\right) \tag{28}$$

where c_s is a numerical coefficient set to 0.22 whereas for the subgrid energy model, the diffusion term is reduced to the simple relation

$$J_{sgs} = \frac{\partial}{\partial x_j}\left[\left(\nu + \frac{c_\nu}{\sigma_k}\frac{k^2_{sgs}}{\epsilon_{sgs}}\right)\frac{\partial k_{sgs}}{\partial x_j}\right] \tag{29}$$

with the usual values of constants $c_\nu = 0.09$ and $\sigma_k = 1.0$. In contrast with the two-equation model using the Boussinesq hypothesis, one can notice that the production term $(P_{ij})_{sgs}$ is allowed to become negative. In such a case, this implies that energy is transferred from the filtered motions up to the resolved motions, known as backscatter process.

2.5 Modelling of the transport equation for the subgrid dissipation rate

Closure of equation (19) needs the modelling of the subgrid tensorial dissipation rate $(\epsilon_{ij})_{sgs}$. In the present approach, like in the statistical modelling, [26], the subgrid tensorial dissipation rate is decomposed into an isotropic part $2/3\epsilon_{sgs}\delta_{ij}$ and an anisotropic part $(\epsilon_{ij})_{sgs} - 2/3\epsilon_{sgs}\delta_{ij}$. Assuming that the anisotropic part has been already incorporated in the modelling of the redistribution term $(\Psi_{ij})_{sgs}$ [26], the question is then to model the energy dissipation rate ϵ_{sgs} which deserves a particular attention in subgrid-scale models. Usually, most of subgrid models based on transport equations of the subgrid-scale energy assume equilibrium turbulence and this hypothesis allows to evaluate the dissipation rate by an algebraic expression referring to the mesh size. In this line of thought, Deardorff [14] proposed a transport equation for the subgrid-scale stress whereas other authors [15, 25] have developed models based on the transport equation for the subgrid-scale energy, each model requiring an algebraic relation for the dissipation rate. In the present approach, closure of equation (19) is made by modelling the subgrid dissipation rate by means of its transport equation without using directly the grid information. Indeed, for high Reynolds numbers flows with coarse meshes and for rapidly evolving flows, the production rate of turbulence does not exactly balance the dissipation rate, and the filter width is no longer a good estimate of the characteristic turbulence length scale, as shown by Da Silva and Pereira [12]. The main advantage of this approach is to allow simulations of non-equilibrium flows when the energy spectrum departs significantly from the Kolmogorov law. The present modelling approach of the subgrid scale dissipation rate finds its basic foundations in spectral space by considering the transport equation of the two-point tensor correlation $\phi_{ij} = \left\langle \widehat{u'}_i(\boldsymbol{x},\boldsymbol{\kappa})\widehat{u'}_j(\boldsymbol{x},\boldsymbol{\kappa})\right\rangle$, where $\widehat{u'}_i$ denotes the Fourier transform of the fluctuating velocity u'_i [9]. Partial integration after spectral splitting gives rise to the dissipation equation, after some algebra. As a result of the analytical development, taking also into account the convective and diffusive processes for nonhomogeneous flows, the fluctuating modelled transport equation in time and space for the subgrid dissipation rate ϵ_{sgs} finally reads [42, 8]

$$\frac{D\epsilon_{sgs}}{Dt} = c_{sgs\epsilon_1}\frac{\epsilon_{sgs}}{k_{sgs}}\frac{(P_{mm})_{sgs}}{2} - c_{sgs\epsilon_2}\frac{\epsilon_{sgs}^2}{k_{sgs}} + (J_\epsilon)_{sgs} \tag{30}$$

where the coefficient $c_{sgs\epsilon_1}$ is found to take the theoretical value 3/2 whereas the coefficient $c_{sgs\epsilon_2}$ appearing in equation (30) now involves the spectral flux $\mathcal{F}(\kappa_d)$ entering the zone delimited by the wave number κ_d located at the end of the inertial range and also the spectrum energy density $E(\kappa_d)$ as follows [42, 8]

$$c_{sgs\epsilon_2} = c_{sgs\epsilon_1} - \frac{\langle k_{sgs}\rangle}{\kappa_d E(\kappa_d)}\left(\frac{\mathcal{F}(\kappa_d)}{\epsilon} - 1\right) \tag{31}$$

The same analytical development can be used to provide the derivation of the dissipation rate equation used in RANS modelling

$$\frac{D\epsilon}{Dt} = c_{\epsilon_1}\frac{\epsilon}{k}\frac{P_{mm}}{2} - c_{\epsilon_2}\frac{\epsilon^2}{k} + J_\epsilon \tag{32}$$

where the coefficient c_{ϵ_1} takes the value 3/2 and the coefficient c_{ϵ_2} is evaluated from the spectral flux [42, 8]

$$c_{\epsilon_2} = c_{\epsilon_1} - \frac{k}{\kappa_d E(\kappa_d)}\left(\frac{\mathcal{F}(\kappa_d)}{\epsilon} - 1\right) \tag{33}$$

In these expressions, $\mathcal{F}$ represents in fact the spectral rate of energy transferred into the wavenumber range $[\kappa_d, +\infty]$ by vortex stretching from the wavenumber range $[0, \kappa_d]$. Equation (31) shows that the function $c_{sgs\epsilon_2}$ is a complicated expression which is not easily tractable in this form. However, when comparing equations (31) and (33) in addition with $c_{sgs\epsilon_1} = c_{\epsilon_1}$, one can evaluate the function $c_{sgs\epsilon_2}$ by an equivalent simple and useful expression without loosing generality [8]

$$c_{sgs\epsilon_2} = c_{\epsilon_1} + \frac{\langle k_{sgs}\rangle}{k}\left(c_{\epsilon_2} - c_{\epsilon_1}\right) \tag{34}$$

showing that $c_{sgs\epsilon_2}$ is then a function of the ratio of the subgrid-scale energy to the total turbulent energy. Equation (30) using the relation (34) constitutes the main feature of PITM approaches which is basically different from an URANS (Unsteady Reynolds Averaged Navier-Stokes) approach, although it is fully compatible with it at the limit of vanishing cutoff. Intuitively, one can easily understand that the usual ϵ equation (32) used in statistical modelling in which the whole spectrum is modelled cannot be transposed without modification in LES in which only a part of the spectrum is modelled. This modification is made through a variation of the coefficient $c_{sgs\epsilon_2}$ and so the model is then able to “read ” the size of the grid in order to model only the appropriate portion of the turbulence field. The theory shows however that the $c_{sgs\epsilon_1}$ coefficient remains a constant which has to be close to the theoretical value of 3/2 (see appendix A). Note that the PANS model appears also in this line of thought with great similarities with the PITM approach but imposes however a fixed ratio for the subgrid energy to the total energy [21]. For the subgrid stress model, the diffusion term $(J_\epsilon)_{sgs}$ appearing on the left hand side of equation (30) is modelled assuming a gradient law hypothesis

$$(J_\epsilon)_{sgs} = \frac{\partial}{\partial x_j}\left(\nu \frac{\partial \epsilon_{sgs}}{\partial x_j} + c_\epsilon \frac{k_{sgs}}{\epsilon_{sgs}}(\tau_{jm})_{sgs}\frac{\partial \epsilon_{sgs}}{\partial x_m}\right) \tag{35}$$

where the coefficient c_ϵ is set to 0.18 whereas for the subgrid energy model, the diffusion term takes the simple expression

$$(J_\epsilon)_{sgs} = \frac{\partial}{\partial x_j}\left[\left(\nu + \frac{c_\nu}{\sigma_\epsilon}\frac{k_{sgs}^2}{\epsilon_{sgs}}\right)\frac{\partial \epsilon_{sgs}}{\partial x_j}\right] \tag{36}$$

with the usual value $\sigma_\epsilon = 1.3$.

2.6 Improved spectral model

As shown in the preceding section, the function $c_{sgs\epsilon_2}$ requires the analytical calculation of the ratio k_{sgs}/k that appears in equation (34). In the present PITM formulation, this ratio is now evaluated by means of an accurate energy spectrum $E(\kappa)$ inspired from a Von Kármán like spectrum valid on the entire range of wavenumbers [10]

$$E(\kappa) = \frac{\frac{2}{3}\beta_\eta L_e^3\, k\, \kappa^2}{\left[1 + \beta_\eta(\kappa\, L_e)^3)\right]^{11/9}} \tag{37}$$

where β_η is a constant coefficient. At the origin, the spectrum behaves like $E(\kappa) = \propto \kappa^2$ taking into account the hypothesis of permanence of very large eddies. The use of this new spectrum (37) valid in the entire range of wavenumbers evolving from large to small eddies allows to obtain a more accurate result for the ratio k_{sgs}/k than the one obtained by the previous formulation referring to the Kolmogorov law only valid in the inertial range $E(\kappa) = C_K \epsilon^{2/3}\kappa^{-5/3}$ [8]. Moreover, we will see that the use of the Von Kármán spectrum provides a new expression for $c_{sgs\epsilon_2}$ which satisfies automatically the limiting conditions when the subgrid energy approaches the total energy. In practice, this situation occurs when performing very large eddy simulations on coarse grids implying that the cutoff wave number may happen to be located before the inertial zone. Due to its definition, the subgrid-scale turbulent kinetic energy is computed by integrating the spectrum $E(\kappa)$ defined by equation (37) in the wave number range $[\kappa_c, +\infty[$. The integration then yields the result

$$\langle k_{sgs}\rangle(\kappa_c) = \int_{\kappa_c}^{\infty} E(\kappa)\, d\kappa = \frac{k}{\left[1 + \beta_\eta(\kappa_c\, L_e)^3)\right]^{2/9}} \tag{38}$$

When considering equation (38) for computing the ratio $\langle k_{sgs}\rangle/k$ which appears in equation (34), one can obtain easily the new analytical expression for $c_{sgs\epsilon_2}$, as a function of the dimensionless cutoff wave number η_c

$$c_{sgs\epsilon_2}(\eta_c) = c_{\epsilon_1} + \frac{c_{\epsilon_2} - c_{\epsilon_1}}{\left[1 + \beta_\eta\, \eta_c^3\right]^{2/9}} \tag{39}$$

The relation (39) shows that the coefficient $c_{sgs\epsilon_2}$ acts like a dynamical parameter which controls the spectral distribution of turbulence through the parameter η_c depending on the turbulent length-scale and on the cutoff wave number defined in equation (26). Note that in contrast

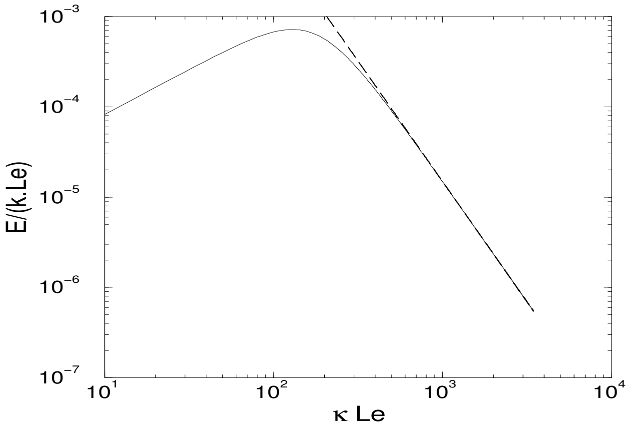

Figure 1: Analytical energy spectrum. - - -: $E(\kappa)/kLe = C_K(\kappa L_e)^{-5/3}$; —: $E(\kappa)/kL_e = \frac{2}{3}\beta(L_e\kappa)^2/\left[1+\beta(\kappa\, L_e)^3)\right]^{11/9}$

with the simplified formulation derived from $\langle k_{sgs}\rangle/k = (3C_K/2)\,\eta_c^{-2/3}$ proposed in reference [8] for wall bounded flows, the new expression (39) automatically verifies the limiting behaviour $lim\ _{\eta_c\to 0}(\langle k_{sgs}\rangle/k)(\eta_c) = 1$ without any additional empirical limiter. On the other hand, when $lim\ _{\eta_c\to\infty}(\langle k_{sgs}\rangle/k)(\eta_c) = 0$, the coefficient $c_{sgs\epsilon_2}$ goes to c_{ϵ_1}. In this case, the subgrid-energy can not be maintained because the computation switches to DNS (or under resolved DNS if the grid-size is not enough refined). In equation (39), the presence of the parameter η_c defined by equation (26) involving the total turbulent energy shows a strong coupling interaction between the subgrid dissipation rate equation (30), the subgrid-scale stress transport equation (19) and the filtered momentum equation (3) since $c_{sgs\epsilon_2}(\eta_c)$ governs the ratio of the subgrid energy to the total energy, as indicated by equation (34). The computation of the function $c_{sgs\epsilon_2}$ requires the knowledge of the coefficient β_η appearing in equation (39). The β_η value can be obtained by satisfying the correct asymptotic behaviour for the spectrum $E(\kappa)$ defined in equation (37), $\lim_{\kappa\to\infty} E(\kappa) = C_K\epsilon^{2/3}\kappa^{-5/3}$ in order to recover the Kolmogorov law at high wavenumbers. In particular, it can be seen that

$$\lim_{\kappa\to\infty} E(\kappa) = \frac{2}{3}k\,\beta_\eta^{-2/9}L_e^{-2/3}\kappa^{-5/3} = \frac{2}{3}\,\beta_\eta^{-2/9}\epsilon^{2/3}\kappa^{-5/3} \tag{40}$$

showing that the coefficient β_η is found to take on the theoretical value $\beta_{\eta\mathcal{T}} = (2/3C_K)^{9/2} \approx 0.026$. Figure 1 describes the evolution of the analytical dimensionless spectrum $E(\kappa)/(kL_e)$ defined by the relation (37) compared to the Kolmogorov slope with $C_K\epsilon^{2/3}\kappa^{-5/3}$, versus the dimensionless wave number $\eta = \kappa\, L_e$. One can see that the analytical spectrum slope goes to the Kolmogorov slope for high wave numbers suggesting that the inertial zone is rapidly reached. In practice, several trial and error tests have been made for selecting appropriate values for the two model coefficients α_η and β_η. These tests have lead to the optimised coefficient values $\beta_\eta = (2/3C_K)^{9/2} \approx 0.0495$ which corresponds to the approximate Kolmogorov value $C_K = 1.3$ and $\alpha_{\eta 1} = 1.3/(20)^2$, $\alpha_{\eta 2} = 1/(20)^2$.

Functions	Expressions
R_t	$k_{sgs}^2/(\nu\epsilon_{sgs})$
c_1	$1+2.58AA_2^{\frac{1}{4}}\,[1-\exp(-(R_t/150)^2)]$
c_2	$0.6A^{\frac{1}{2}}$
c_{1w}	$-\frac{2}{3}c_1+\frac{5}{3}$
c_{2w}	$\max(\frac{2}{3}c_2-\frac{1}{6},0)/c_2$
f_w	$0.4k_{sgs}^{3/2}/\epsilon_{sgs}x_n$
η_c	$(\pi\,k^{3/2})/[(\Delta_1\Delta_2\Delta_3)^{1/3}\;(\epsilon_{sgs}+\epsilon^{<})]$
c_{sgs_1}	$c_1(1+\alpha_{\eta 1}\,\eta_c^2)/(1+\alpha_{\eta 2}\,\eta_c^2)$
$c_{sgs\epsilon_2}$	$c_{\epsilon_1}+[(c_{\epsilon_2}-c_{\epsilon_1})/\,(1+\beta_\eta\,\eta_c^3)^{2/9}\,]$

Table 1: Functions used in the subgrid stress model.

Relatively to the theoretical value, the β_η value was modified for modelling roughly 1/3 of subgrid-scale energy for 2/3 of resolved-scale energy when performing LES simulations on coarse grids typically encountered in engineering applications. In the other hand, the coefficients $\alpha_{\eta 1}$ and $\alpha_{\eta 2}$ have been estimated in analogy with multiple scale modelling [38]. The present Reynolds stress PITM model based on the transport equations (19) and (30) is sensitised to the cutoff location and it can be extended to low Reynolds number flows. This is important for properly capturing the mean velocity and turbulent stresses in the wall boundary layer, as indicated in appendix A with the functions listed in Table (1). Furthermore, it will be demonstrated in appendix B that the subgrid stress model is able to satisfy the realisability conditions in homogeneous flows when the turbulence production is positive. But this is not guaranteed in all number of circumstances, especially for instance when the cutoff wave number is located in low wave numbers in region of high compressive strain.

2.7 Limiting behaviour for the subgrid energy model

This section is concerned with the asymptotic behaviour of the subgrid energy model defined by equations (20) and (30) when the cutoff location approaches the upper or the lower limits of the energy spectrum wavenumber interval. When the parameter η_c goes to zero, $c_{sgs\epsilon_2}$ goes to usual c_{ϵ_2} and the model behaves like a RANS model. For LES performed on very large filter widths, i.e. with small cutoff wavenumbers, one can remark that the filter width needs to be dissociated from the grid itself. The reason is that the grid must always be fine enough to capture the mean flow non-homogeneities. Then, the model tends continuously to the corresponding statistical model. On the contrary, when η_c goes to infinity, the coefficient $c_{sgs\epsilon_2}$ goes to c_{ϵ_1}. In this case, the subgrid-energy can not be maintained because the computation switches to DNS (or an under resolved DNS if the grid-size is not enough refined). In this case P_{sgs} is then equal to ϵ_{sgs} : this represents the local equilibrium situation inside a very small slice in the far end of the energy spectrum. But remark that this limit has no practical interest, because the model becomes useless when reaching the DNS level! When the filter width is small, i.e. when the cutoff wavenumber is large but not infinite, it is possible to find a limiting intermediate behaviour. In a first step, it is useful to develop the length scale $\langle k_{sgs}\rangle^{3/2} / \langle\epsilon_{sgs}\rangle$ using the ratio $\langle k_{sgs}\rangle / k$

$$\frac{\langle k_{sgs}\rangle^{3/2}}{\langle\epsilon_{sgs}\rangle} = \frac{k^{3/2}}{\langle\epsilon_{sgs}\rangle}\left(\frac{\langle k_{sgs}\rangle}{k}\right)^{3/2} \tag{41}$$

Assuming that the cutoff is located near the upper range inside the inertial zone and taking into account the limiting value $\langle k_{sgs}\rangle / k \approx (3C_K/2)\,\eta_c^{-2/3}$ obtained in spectral equilibrium situation when $\langle k_{sgs}\rangle \ll k$, equation (42) shows that the subgrid characteristic length scale goes to the filter width

$$\frac{\langle k_{sgs}\rangle^{3/2}}{\langle\epsilon_{sgs}\rangle} = \frac{\Delta}{\pi}\left(\frac{3C_K}{2}\right)^{3/2} \tag{42}$$

Moreover, the subfilter viscosity is defined by $\nu_{sgs} = c_\nu(\langle k_{sgs}\rangle^2 / \langle\epsilon_{sgs}\rangle)$ and if one makes use of the ratio $\langle k_{sgs}\rangle^{3/2} / \langle\epsilon_{sgs}\rangle$, then it is possible to write equivalently

$$\nu_{sgs} = c_\nu^{3/2}\left(\langle k_{sgs}\rangle^{3/2} / \langle\epsilon_{sgs}\rangle\right)^2 \left(\langle\epsilon_{sgs}\rangle / \nu_{sgs}\right)^{1/2}. \tag{43}$$

Considering the previous result for the length-scale and assuming equilibrium between the production and the dissipation rate at high Reynolds number, implying $\langle\epsilon_{sgs}\rangle = 2\nu_{sgs}\left\langle\bar{S}_{ij}\bar{S}_{ij}\right\rangle$ with $\bar{S}_{ij} = (\partial\bar{u}_i/\partial x_j + \partial\bar{u}_j/\partial x_i)/2$, one can find that the limiting behaviour for the subgrid viscosity ν_{sgs}. The first parenthesis in equation (43) goes to the filter width and the second parenthesis goes to the squared deformation. This is indeed the Smagorinsky model with

$$\nu_{sgs} = \frac{1}{\pi^2}\left(\frac{3C_K}{2}\right)^3 c_\nu^{3/2}\Delta^2\left[2\left\langle\bar{S}_{ij}\bar{S}_{ij}\right\rangle\right]^{1/2} \tag{44}$$

This expression is valid at the limiting condition when both the grid-size is very small and the spectral equilibrium is reached, otherwise a function of dynamical effects would be embodied in equation (43) which takes into account non standard spectral distributions with some departure from the Kolmogorov spectrum, and non-equilibrium like in the case of the dynamic model [19].

3 Numerical method

The numerical code [3] is based on a finite volume technique which is well appropriate for solving the full transport equations. The governing equations under conservative form are integrated explicitly in time using a fourth-order Runge-Kutta scheme which is well suited for simulating unsteady flows. An implicit scheme in time is however applied for solving the turbulent source terms that evolve rapidly in time and space because of the increasing mathematical complexity arising from nonlinearity and interaction from the coupling of equations [10]. Two different schemes in space have been applied for the aerodynamic and the turbulent variables, respectively. For the aerodynamic variables, a numerical scheme based on a centred formulation with second-order or fourth-order accuracy in space has been retained with a flux limiter used for suppressing the spurious numerical oscillations. Whereas for the turbulent variables, $(\tau_{ij})_{sgs}$ and ϵ_{sgs}, an upwind scheme with second order accuracy in space has been considered. This numerical procedure has been developed in order to ensure positive values of the normal stresses at each time advancement of the simulation in addition to the realisability conditions of the model, so that no artificial limiter was required. In practice, several numerical attempts showed that the second and fourth-order schemes in space discretisation provided quasi-similar solutions. But the order of the scheme discretisation in time was found to have a major impact on the solutions, especially when simulating the decay of homogeneous isotropic turbulence. Finally, these combined space-time methods have been retained because of their properties that minimise the dissipative and dispersive numerical errors. One obtained a high resolution scheme allowing accurate simulations of the resolved scales, as it will be shown in the next sections when illustrating the results of the decay of homogeneous isotropic turbulence and the channel flow simulations. More details of the numerical method are provided in reference [3].

4 Simulation of homogeneous turbulence using the subgrid-energy model

4.1 Decay of an isotropic non-perturbed spectrum

The present PITM model is first tested in its two-equation contracted form defined by equations (20) and (30) in the case of decay of homogeneous isotropic turbulence referring to the experiment of Comte-Bellot [11] in order to check the behaviour of the model (not concerned with the anisotropy aspects). Three-dimensional turbulent energy spectra have been measured in [11] at different distances from the grid (reported in terms of time advancement in the numerical calculation) and the initial Reynolds number $R_t = k^2/(\nu\epsilon)$ is about 800. The PITM simulation is performed on a medium grid $N = 80^3$ for a box-size $L = 1.256$ m. The wave-numbers are defined by $\boldsymbol{\kappa} = 2\pi\,[m, n, p]^t/L$ where m, n, p are integers that vary in the range $[-N/2 + 1, N/2]$ leading to a minimum wave-number $\kappa_{min} = 2\pi/(N\Delta) = 0.05$ cm^{-1} and a maximum wave-number $\kappa_{max} = \pi/\Delta = 2$ cm^{-1}. In the present case, a short cutoff wave-number $\kappa_c = 2$ cm^{-1} is retained in comparison with the maximum wave number of the Comte-Bellot experiment ($\kappa_{max} = 20$ cm^{-1}). In this situation, the initial ratio of the subgrid-scale energy to the total energy k_{sgs}/k is about 0.36 and implies that an appreciable part of the subgrid energy is modelled. The initial velocity field has been produced by a random generator enforcing the given energy spectrum as shown in appendix B. The computations are performed using the fourth-order Runge-Kutta scheme in time and the fourth order centred scheme in space. Note that previous numerical attempts have revealed that it is essential to apply high order schemes in time for obtaining a correct decay law for the spectrum density. In particular, it has been found that the second order Runge-Kutta scheme produced too high dissipation of the energy spectrum, especially in the domain of large wave numbers. Figure 2 shows the evolution of the computed three-dimensional spectra starting from the initial time (tU_0/M =42) for the two values of advancement in time (tU_0/M =98, 171) compared to the Comte-Bellot data. One can observe that the first numerical spectrum computed at the time tU_0/M =98 is in good agreement with the experimental data but the other one computed at the time advancement tU_0/M =171 slightly deviates from the data. In fact, a more thorough

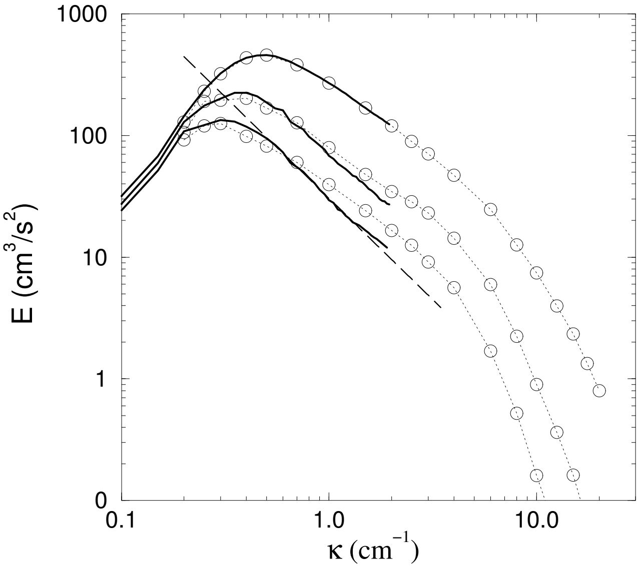

Figure 2: Homogeneous decay of the energy spectra ($\kappa_c = 2$ cm^{-1}). $\cdots$ ○ $\cdots$: Comte-Bellot experiment ($t\,U0/M$ =42, 98 and 171); - - : Kolmogorov spectrum with $-5/3$ slope; —: LES simulation.

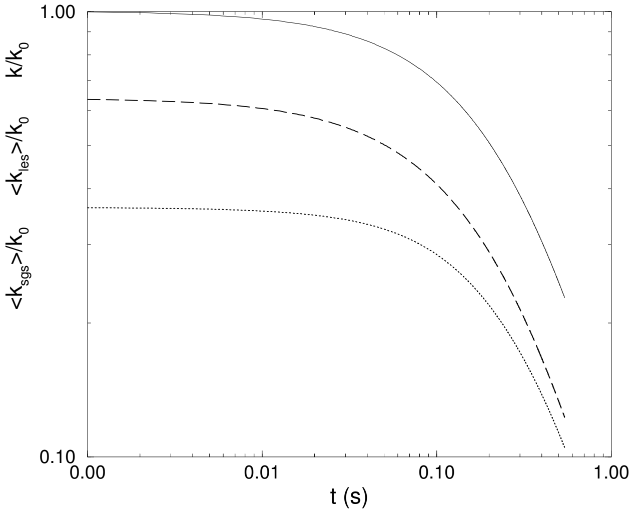

Figure 3: Homogeneous decay of the turbulent kinetic energy. ...: $\langle k_{sgs}\rangle/k_0$; - -: $\langle k_{les}\rangle/k_0$; —: $k/k_0 = (\langle k_{sgs}\rangle + \langle k_{les}\rangle)/k_0$.

investigation reveals that the numerical slope computed at tU_0/M =171 exactly corresponds to the $\kappa^{-5/3}$ Kolmogorov slope, as shown in this figure. This slight disagreement between the LES and the experiment can be physically explained by the fact that the experiment is worked out at a relatively low Reynolds number ($R_t = 792$), implying that the inertial transfer zone for the energy cascade is very short in comparison with standard inertial zones computed at higher Reynolds numbers. Figure 3 shows the time decay of the turbulence, respectively for the subgrid-scale energy $\langle k_{sgs} \rangle$, the resolved-scale energy $\langle k_{les} \rangle$ and the total energy in logarithmic coordinates. The decay law given by the standard $k - \epsilon$ model, according to the relation $k/k_0 = t^{1/(1-c_{\epsilon_2})}$ (where k is obtained in the present LES by the sum of the subgrid and resolved-scales), leads to the slope of decay close to $n = -1.1$ that corresponds to the usual value $c_{\epsilon_2} = 1.90$ used in the statistical dissipation rate equation (32).

4.2 Decay of an isotropic perturbed spectrum

In this case, the initial Comte-bellot spectrum (α) at the advancement time $tU_0/M = 42$ is artificially perturbed by modifying the energy levels in some particular zone of the spectrum thus departing from usual equilibrium distribution, as shown in figure 4. The aim is to study the influence of initial spectral distribution on the decay law as an illustration of out of equilibrium situations. Relatively to the non-perturbed spectrum (α), the initial spectra are therefore modified, respectively, by increasing the large scales (β) or by decreasing the large scales (γ) levels. The PITM results as well as the initial perturbed spectrum are plotted in figure 4. A first observation reveals that the different curves associated to the two perturbed spectra (β) and (γ) are both identical at the very beginning of decay but afterwards they are soon departing from the usual decay curve corresponding to the non-perturbed spectrum (α). As a result of interest, one can observe that a peak in large scale energy (resp. a defect in large scale energy) implies a decrease (resp. an increase) of the decay rate of turbulence. These results are found to be in qualitative agreement with EDQNM (eddy damped quasi-normal Markovian) spectral models predictions [2]. These evolutions can be easily explained if one consider firstly that the curves can only depart from each other after the cascade time delay required for the perturbed area to reach the dissipation zone of the three-dimensional spectrum. Then, the curves deviate from each other because the small scale energy decreases more rapidly than the large scale energy and indeed the smaller the eddies the shorter is their time scale. Obviously, this turbulence spectral effect due to departure from equilibrium cannot be reproduced using standard single scale statistical turbulence models because the whole spectrum is modelled without any splitting allowing to distinguish large and small scales.

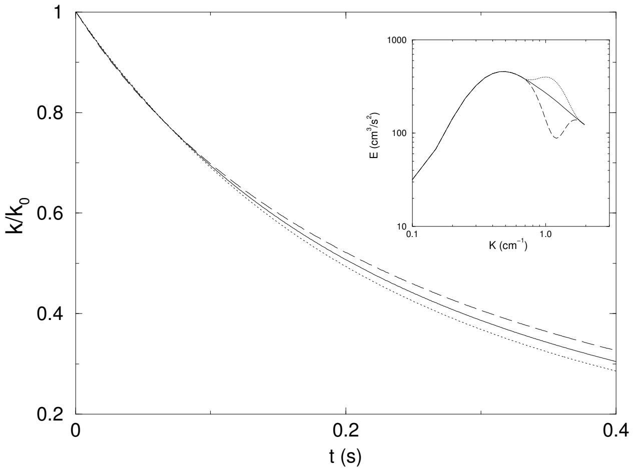

Figure 4: Homogeneous decay of the turbulent energy in situation of perturbed spectrum $k/k_0 = (\langle k_{sgs}\rangle + \langle k_{les}\rangle)/k_0$; $\kappa_c = 2$ cm^{-1}; (α) : —; (β) ...; (γ) - - -.

5 Simulation of non-homogeneous turbulence using the subgrid stress model

5.1 Fully turbulent channel flow

The test case of the fully developed turbulent channel flow is proposed for analysing the potentials of the subgrid-stress model and, especially its capacity to reproduce the flow anisotropy and wall flows. Two different grids are generated with a coarse and a medium spatial resolutions $16 \times 32 \times 64$ and $32 \times 64 \times 84$, respectively in the streamwise, spanwise and normal directions for checking the grid independence of the solutions. A special attention is devoted to the sharing out of the energy between the subgrid-scales and resolved scales of motion when the filter width changes. The sizes of the channel along the axes x_1, x_2, x_3, the number of grid points N_i, the length of the computational box L_i relative to the channel width δ, and the uniform spacings Δ_i (i=1,2) are indicated in Table 2. In the normal direction to the wall, the grid points are distributed using non-uniform spacing with refinement near the wall according to the transformation

$$x_{3j} = \frac{1}{2} \tanh \left[\xi_j \operatorname{atanh} a\right] \tag{45}$$

where

$$\xi_j = -1 + 2(j-1)/(N_3 - 1) \ (j = 1, 2, \cdots N_3) \tag{46}$$

$a = 0.98346$ and $N_3 = 64$ or 84. The grids are uniform in the two remaining directions. The first grid point in the direction normal to the wall is located at the dimensionless distance $\Delta_3^+ = \Delta_3 \, u_\tau/\nu = 0.5$ for the coarse mesh and $\Delta_3^+ = 0.3$ for the refined mesh whereas the uniform dimensionless spacings in the other directions are $\Delta_1^+ = 105.3$, $\Delta_2^+ = 50.9$ for case 1 and $\Delta_1^+ = 50.9$, $\Delta_2^+ = 25.1$ for case 2. The subgrid model is applied here in a low Reynolds number version in the

Case	N_1	N_2	N_3	L_1/δ	$L_{i=2,3}/\delta$	Δ_1/δ	Δ_2/δ	Δ_{3c}/δ	Δ_1^+	Δ_2^+
DNS [34]	256	192	193	π	$\pi/2$	0.012	0.008	0.008	10.0	6.5
present LES 1	16	32	64	2	2	0.133	0.065	0.038	105.3	50.9
present LES 2	32	64	84	2	2	0.065	0.032	0.029	50.9	25.1

Table 2: Simulation parameters for the fully developed turbulent channel flow.

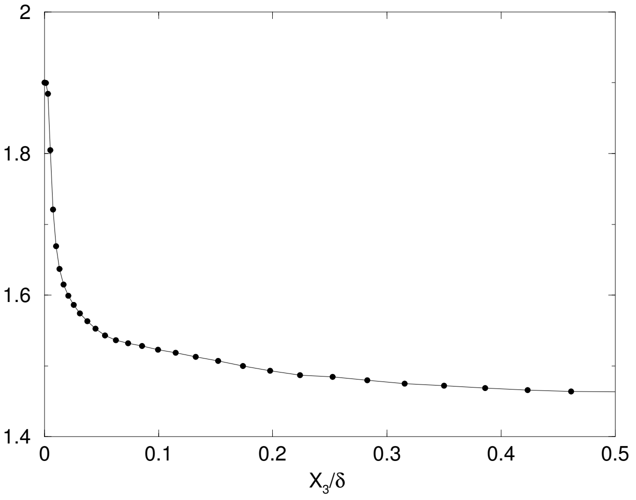

Figure 5: Subgrid-scale coefficient $c_{sgs\epsilon_2} = c_{\epsilon_1} + [(c_{\epsilon_2} - c_{\epsilon_1})/\left(1 + \beta_\eta\, \eta_c^3\right)^{2/9}]$ ●, LES 1 (16 × 32 × 64). $R_\tau = 395$.

aim to calculate the near wall flow region. In particular, like in the Launder and Shima model [26], the influence of anisotropy invariants is introduced (see appendix A).

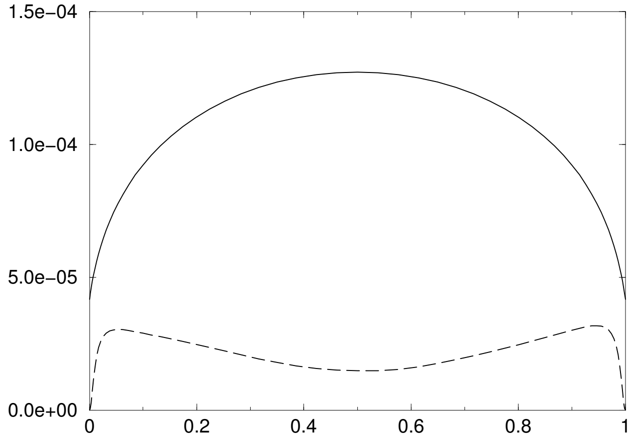

Figure 6: Subgrid length scale —: $\Delta = \pi/\kappa_c$; - - -: $L_{sgs} = \pi(3C_K/2)^{-3/2} \langle k_{sgs}\rangle^{3/2} / \langle \epsilon_{sgs}\rangle$; LES 1 ($16 \times 32 \times 64$)

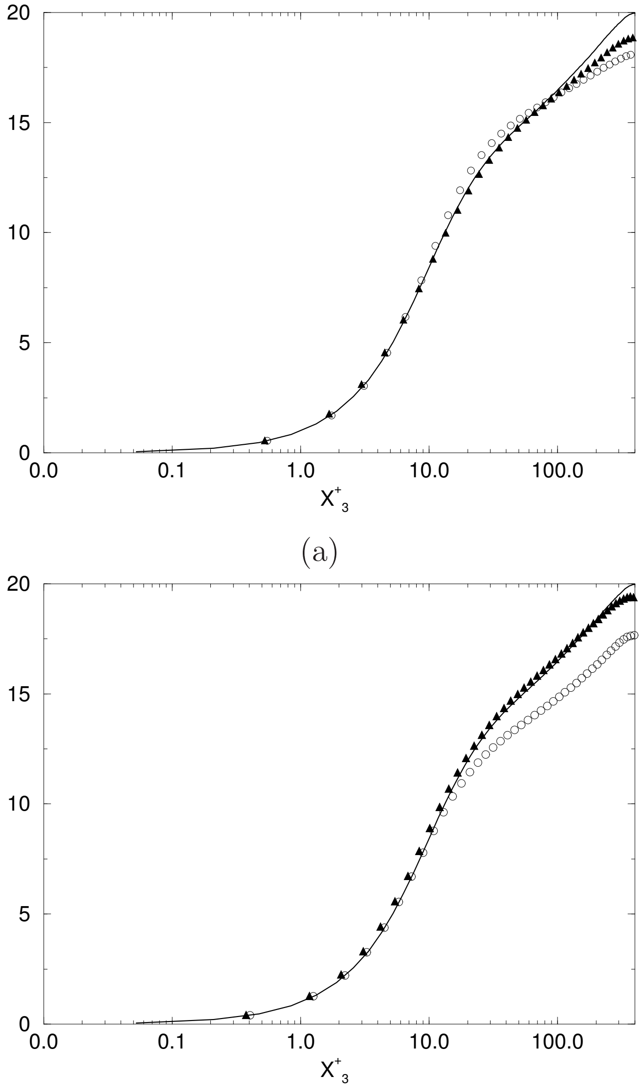

(a)

(b)

Figure 7: Mean velocity profile. $\langle u_1 \rangle / u_\tau$ in logarithmic coordinate; (a), LES 1 ($16 \times 32 \times 64$). (b), LES 2 ($32 \times 64 \times 84$). LES : ▲; Smagorinsky: ○; DNS :—; $R_\tau = 395$.

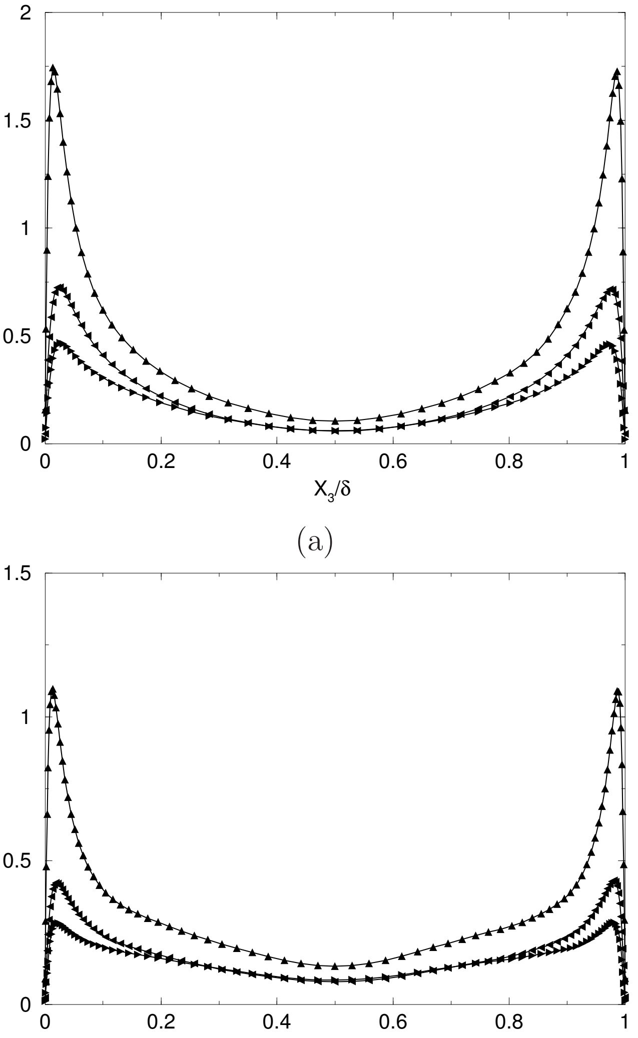

(a)

(b)

Figure 8: Turbulent subgrid scale stresses $\langle(\tau_{ii})_{sgs}\rangle^{1/2}/u_\tau$. (a), LES 1 ($16 \times 32 \times 64$). (b), LES 2 ($32 \times 64 \times 84$). ▲: i=1; ◀:, i=2; ▶:, i=3.

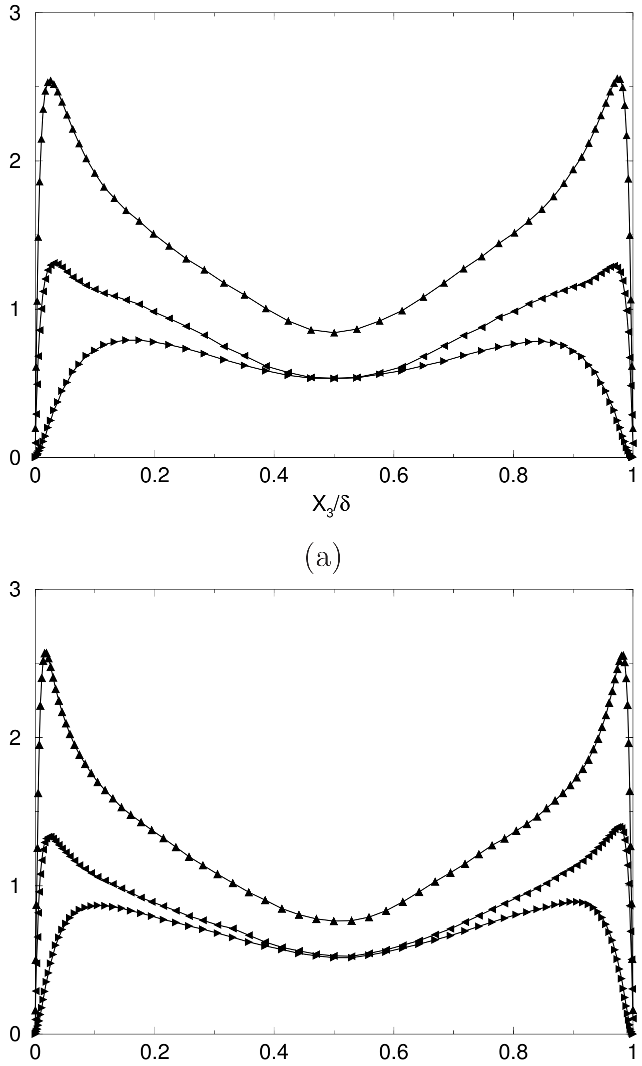

Figure 9: Turbulent resolved scale stresses $\langle(\tau_{ii})_{les}\rangle^{1/2}/u_\tau$. (a), LES 1 ($16 \times 32 \times 64$). (b), LES 2 ($32 \times 64 \times 84$). ▲: i=1; ◀: i=2; ▶: i=3.

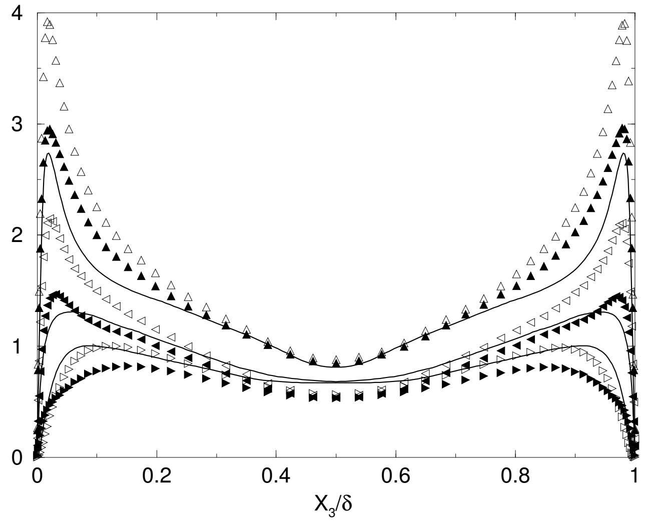

(a)

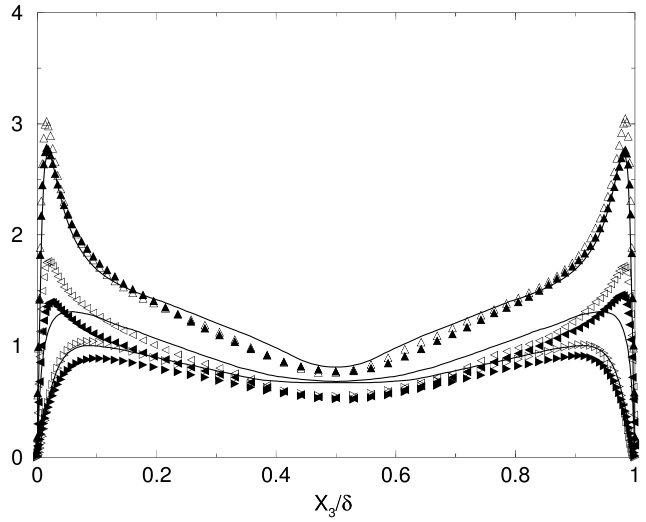

(b)

Figure 10: Turbulent Reynolds stresses $(\langle(\tau_{ii})_{sgs}\rangle + \langle(\tau_{ii})_{les}\rangle)^{\frac{1}{2}}/u_\tau$. (a), LES 1 ($16 \times 32 \times 64$). (b), LES 2 ($32 \times 64 \times 84$). LES : ▲: i=1; ◀: i=2; ▶: i=3; Smagorinsky : △: i=1; ◁: i=2; ▷: i=3; DNS :—; $R_\tau = 395$.

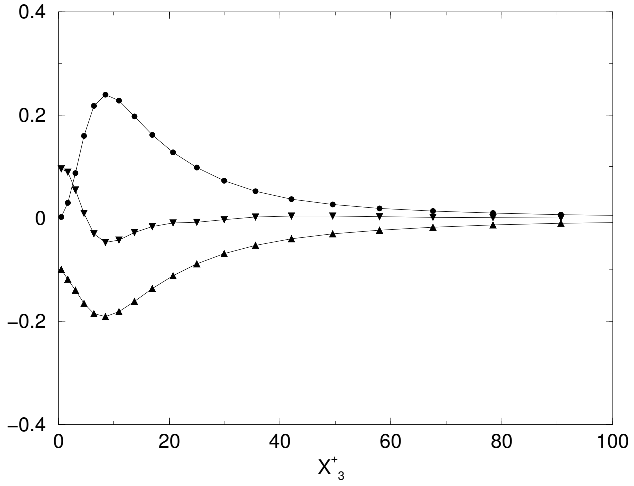

Figure 11: Terms in the energy balance equation (20) of the subgrid-scale energy versus the logarithmic coordinate; LES 1 ($16 \times 32 \times 64$). $\bullet : \nu P_{sgs}/u_\tau^4$; $\blacktriangledown : \nu J_{sgs}/u_\tau^4$; $\blacktriangle : -\nu \epsilon_{sgs}/u_\tau^4$; $R_\tau = 395$

.

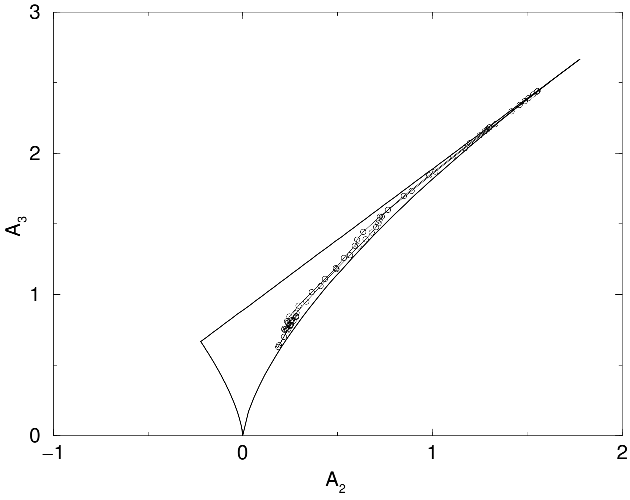

Figure 12: Solution trajectories projected onto the plane formed by the second subgrid-scale invariant $A_2 = a_{ij}a_{ji}$ and the third subgrid-scale invariant $A_3 = a_{ij}a_{jk}a_{ki}$. ○: LES 1 ($16 \times 32 \times 64$). $R_\tau = 395$.

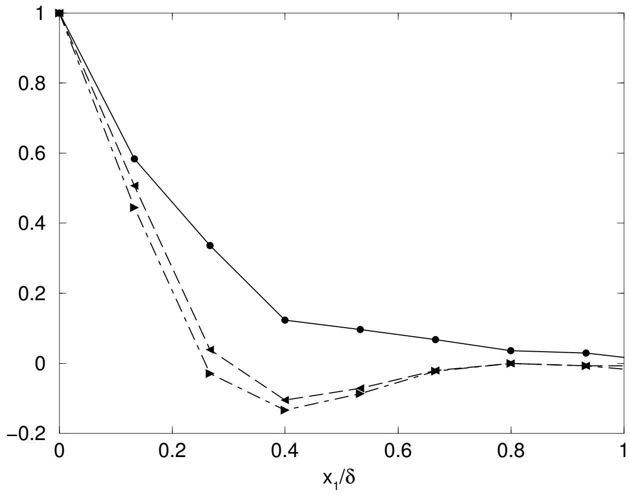

Figure 13: Streamwise two-point correlation function. — R_{11}; $- -$ R_{22}; $-. -$ R_{33}. $x_3^+ = 390$, $x_3 = \delta$; LES 1 ($16 \times 32 \times 64$). $R_\tau = 395$.

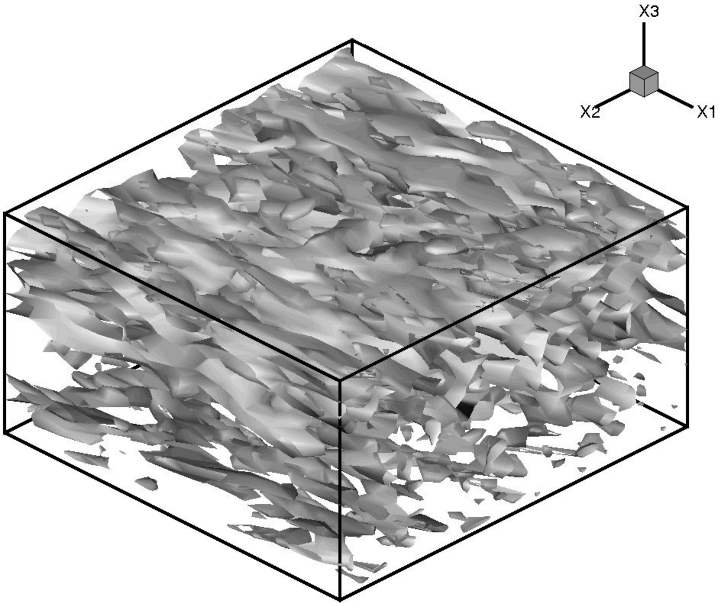

Figure 14: Isosurfaces of instantaneous vorticity vector in the streamwise direction $\omega_1 \nu / u_\tau^2 = 0.04$. LES 1 ($16 \times 32 \times 64$)

.

The LES results are compared with the data of the direct numerical simulation performed by Moin et al. [34] at a Reynolds number $R_\tau = 395$, based on the friction velocity u_τ and the channel half width $\delta/2$, mainly for the velocity and the total turbulent stresses obtained from the sum of the subgrid and large scales energies. The boundary conditions applied to the computational domain are periodic boundary conditions in the streamwise and spanwise directions and a no slip velocity condition at the walls. A constant pressure gradient term has been implemented in the momentum equation (3) for balancing the friction at the walls. For comparison purposes, numerical LES simulations using the Smagorinsky model in a version proposed by Lilly [29] are also performed. This variant model takes into account the mean strain rate instead of the instantaneous filtered strain as follows

$$\nu_t = (C_s D\, \Delta)^2 \left\langle 2\bar{S}_{ij}\bar{S}_{ij} \right\rangle^{1/2} \tag{47}$$

where D is Van Driest Damping function defined by $D = 1 - \exp(x_3^+/25)$ and C_s is the Smagorinsky constant taken to the consensual value 0.1.

Figure 5 shows the evolutions of the function $c_{sgs\epsilon_2}$ versus the wall distance x_3 for the mesh with coarse spatial resolution. According to equation (39), it is found that $c_{sgs\epsilon_2}$ varies in the range $[c_{\epsilon_1}, c_{\epsilon_2}]$. In particular, this function $c_{sgs\epsilon_2}$ goes to the upper limit c_{ϵ_2} near the walls and approaches the lower limit c_{ϵ_1} when moving to the centreline of the channel. Physically, this result means that the subgrid-scale model varies continuously from quasi-URANS to a LES model and behaves more or less like the RSM model near the wall, although the mesh is very refined ($\Delta_3^+ = 0.5$). The main reason that explains such behaviour is due to the dynamical parameter $\eta_c = \kappa_c L_e$ that can be viewed as the ratio of the turbulent length-scale to the grid-size $\pi L_e/\Delta$ and which goes to zero near the wall region implying a RANS model behaviour. This is not a property of the model but the consequence of a particular choice in grid refinement. Moreover, one has to keep in mind that the energy spectrum shape is not universal and is locally evolving in time and space. Considering that the spectrum near the wall region is out of spectral equilibrium, the subgrid-scale energy may be very large in the wall region, even for a large cutoff wave number. Figure 6 shows the profiles of the grid size $\Delta = \pi/\kappa_c$ as well as the computed turbulent length scale $L_{sgs} = \pi(3C_K/2)^{-3/2} \langle k_{sgs}\rangle^{3/2} / \langle \epsilon_{sgs}\rangle$ given by equation (42) versus the wall distance in the channel for the simulation performed on the coarse mesh. One can see that these two scales differ from each other, confirming the necessity to evaluate the length-scale by means of its subgrid dissipation-rate equation (30) instead of simply assuming an equilibrium hypothesis. Figure 7 shows the profiles of the statistical mean velocity $\langle u_1\rangle / u_\tau$ in logarithmic coordinate $x_3^+ = x_3 u_\tau/\nu$ for the simulations performed on the coarse and refined meshes, respectively. As a result, it is found that both velocities computed by the subgrid-stress model agree very well with the DNS data. This result was expected since the velocity profile is mainly governed by the model that behaves like the RSM model in the wall region, provided the low Reynolds number formulation is sufficiently accurate. On the contrary, the Smagorinsky velocities present some deviations with the DNS data in the logarithmic region. Figure 8 displays the evolutions of the streamwise, spanwise and normal normalised subgrid stresses, $\langle (\tau_{ii})_{sgs}\rangle^{1/2} / u_\tau$ for the coarse and refined meshes. One can see that the subgrid scale stresses are indeed anisotropic in the vicinity of the walls. As already mentioned, only a second order closure modelling is able to reproduce the flow anisotropy because of the pressure-strain term $(\Psi_{ij})_{sgs}$ which redistributes the energy among the subgrid-stresses. This remark justifies the present strategy that has discarded viscosity models. Figure 9 shows the evolutions of the resolved stresses $\langle(\tau_{ii})_{les}\rangle^{1/2}/u_\tau$ for both simulations. The resolved stresses present regular shapes characterised by the peaks of turbulence intensity close to the walls. It appears that the statistical convergence has been fully reached as shown by the good degree of symmetry of the curves. The present model, however, requires more temporal iterations than needed in the previous formulation valid for wall bounded flows [8] to reach the flow convergence because of the strong coupling interaction between the subgrid dissipation rate and stress equations. When comparing the stresses between the two LES simulations performed on the coarse and refined meshes, the evidence is clear that the sharing out of the turbulence energies is governed by the grid size. In particular, the subgrid stresses performed on the coarse mesh present higher intensity than those observed for the refined mesh whereas the reverse situation occurs for the resolved stresses. Moreover, one can see that the resolved scales are of higher energy than the subgrid scales in the centre of the channel. This results means that the core flow is strongly characterised by the large scales. Figure 10 describes the evolutions of the normalised total Reynolds stresses computed by the subgrid stress model as the sum of the subgrid and large scale parts $(\langle(\tau_{ii})_{sgs}\rangle + \langle(\tau_{ii})_{les}\rangle)^{1/2}/u_\tau$ (i=1,2,3) for the two LES simulations performed on the coarse and refined meshes. One can observe a good agreement with the DNS data for both coarse and refined grids. In particular, the turbulent peak close to the walls is well reproduced. It appears however that the stresses are slightly overpredicted by the coarse simulation whereas an excellent agreement is observed for the refined simulation. This difference should probably attributed to the numerical scheme diffusion which increases with the width of the grid size. On can see also that the normal stresses computed on the coarse grid using the Smagorinsky model highly overpredict the DNS data although the stresses associated to the refined grid show better agreement with the data. This confirms that the Smagorinsky model requires very refined grids for providing accurate results because of its simple formulation based on equilibrium assumptions.

Figure 11 is concerned with the budget of the subgrid turbulent energy equation (20). This figure shows the evolutions of the subgrid production, diffusion and dissipation terms P_{sgs}, J_{sgs}, ϵ_{sgs} in logarithmic coordinate for the LES simulation performed on the coarse mesh ($16 \times 32 \times 64$). One can see that these terms become important close to the wall and decrease rapidly away the wall. Close to the wall, the subgrid diffusion is of the same level as the subgrid dissipation, showing that the diffusion process plays an important role in the boundary layer, and when moving away from the wall, the diffusion decreases rapidly. For the dimensionless distance $x_3^+ > 30$, the subgrid turbulence production balances the subgrid dissipation rate. At the wall, the molecular diffusion exactly balances the dissipation rate. These information suggest that the meshes used in LES simulations must be sufficiently refined near the walls for correctly reproducing the physical processes acting in the boundary layer, even for industrial flows performed on coarse meshes. In the preceding section, it has been recalled that the subgrid-scale model is able to satisfy the weak form of the realisability conditions. We propose to illustrate this result by considering the diagram of Lumley [30] for a particular case when the solution trajectories are computed along a straight line normal to the wall in a cross section of the channel. The plane formed by the second and third subgrid-scale invariants A_2, A_3 has been considered to check the realisability constraint. In this framework, Lumley [30] has demonstrated that the possible turbulence states must remain inside a curvilinear triangle delimited by the straight line of the two-dimensional state satisfying equation $A_3 - A_2 + 8/9 = 0$ and by two curves of axisymmetric states satisfying equations $|A_2| = 6^{1/3}\, A_3^{2/3}$. Figure (12) shows the computed trajectories in the triangle of Lumley. A first observation reveals that the solution trajectories remain inside the curvilinear triangle of realisability, confirming that the realisability conditions (52), (53) and (54) are satisfied. When moving from the wall toward the centreline of the channel, the trajectories depart from the upper region of the triangle and slowly approach the origin of the triangle, showing that the anisotropy of the turbulence decreases with respect to the wall distance of the channel. The channel flow investigation is followed by figure 13 which describes the evolutions of two-point correlation tensors

$$R_{ii}(x_1, x_2, x_3) = \frac{\langle u_i^<(x_1, x_2, x_3) u_i^<(x_1 + r_1, x_2, x_3)\rangle}{\left\langle u_i^{<2}(x_1, x_2, x_3)\right\rangle} \tag{48}$$

for $i = 1, 2, 3$ (no summation), R_{11}, R_{22} and R_{33}, versus the streamwise distance x_1 where r_1 ranges from 0 to δ for the simulation performed on the coarse mesh. The two-point correlations of the resolved scales are computed using the relation (10). The correlations are plotted for (x_1, x_2, x_3) located on the centreline of the channel $x_3 = \delta$ where the resolved scale energy is much larger than the subgrid scale energy. Firstly, it can be observed that the box size is adequate since the longitudinal two-point correlation tensor almost returns to zero. Secondly, it is found that the velocity correlation R_{11} in the streamwise direction is larger than the corresponding transverse correlations R_{22} or R_{33}. As usually known, the slow decay of R_{11} with respect to the distance r_1 indicates the presence of highly elongated eddies in the streamwise direction [33]. It is remarkable that the present calculation, in spite of its coarse grid resolution in the centre of the channel, succeeded to provide a good qualitative evolution of the two-point correlation tensor. Note that other turbulent variables involving two-point velocity correlations such as for instance the tensorial length-scale in each direction can also be computed from the present simulation. Figure 14 shows the isosurfaces of the instantaneous vorticity vector in the streamwise direction indicating the dynamical elements of the flow in wall turbulence. Although the grid is relatively coarse, the simulation reproduces qualitatively these structures according to DNS data [33]. In particular, the elongated eddies are well observed in the streamwise direction.

6 Concluding remarks

The PITM approach viewed as a continuous hybrid RANS/LES model has been reconsidered using a general formulation based on an accurate analytical energy spectrum $E(\kappa)$ inspired from Von Kármán spectra that can be used on the entire range of wavenumbers. Also, a characteristic turbulence length scale $L_e = k^{3/2}/(\langle\epsilon_{sgs}\rangle + \langle\epsilon^<\rangle)$ computed at each time advancement is introduced in order to apply to low Reynolds number turbulence in which the viscous dissipation in the resolved scales is not negligible. The main hypotheses underlying the development of the method have been specified. Beyond the formal analogy in the equations, from a physical point of view, it is assumed in the LES framework that the interaction mechanisms of the subgrid-scales with the resolved scales of the turbulence are of the same nature than the interaction mechanisms involving all the fluctuating scales with the mean flow, allowing transposition of closure hypotheses from RANS to

LES. This model has been calibrated and successfully tested on the decay of homogeneous isotropic turbulence referring to the well known Comte-Bellot experiment. Then it has been applied to the case of an homogeneous non-equilibrium flow generated artificially by perturbing the initial energy spectrum. A correct qualitative behaviour has been obtained in agreement with EDQNM predictions. The performance of the model and especially, its capabilities in the prediction of strong nonhomogeneities and anisotropies have been demonstrated in the fully turbulent channel test flow case. It has been shown that the PITM method allows to perform numerical simulations of turbulent flows on coarse meshes, whatever the location of the cutoff wave number. The method is fully compatible with the usual RANS models which appear as the limit of the model when the cutoff vanishes. The present hybrid RANS/LES model looks as a good candidate for studying engineering turbulent flows that presents complex physics, going beyond the usual URANS approaches provided however that the numerical solver for the transport equations is sufficiently stable and accurate for reproducing the unsteady large scales of the flow. As examples of engineering illustration, the subgrid-scale energy was successfully applied for simulating both a channel flow subjected to periodic forcing [42] and a spatial development of a shearless mixing layer involving non-equilibrium spectral distributions [1]. The subgrid scale stress model in a previous version was used for simulating a channel flow with mass injection subjected to the development of natural unsteadiness leading to a transition regime, and a good description of the flow was obtained [8]. The present subgrid-scale stress model will be considered soon for predicting a separated flow in a channel with streamwise periodic constrictions for purpose of comparison with refined LES [16]. In the near future, more various extensive applications will be necessary to assess more thoroughly the PITM potentials for practical applications. In particular calculations with well documented recirculating flows like the constricted channel flow would be interesting. Another direction of research would be natural or forced unsteady behaviours.

A Appendix: Low Reynolds number formulation of the subgrid-scale stress model

The present subgrid stress PITM model based on the transport equations (19) and (30) is developed in a low Reynolds number formulation. Like in the Launder and Shima model [26], the function c_1 in equation (24) depends on the second and third subgrid-scale invariants $A_2 = a_{ij}a_{ji}$, $A_3 = a_{ij}a_{jk}a_{ki}$ and the flatness parameter $A = 1 - \frac{9}{8}(A_2 - A_3)$ where $a_{ij} = [(\tau_{ij})_{sgs} - \frac{2}{3}k_{sgs}\delta_{ij}]/k_{sgs}$. For isotropic flows, the parameter A goes to unity since the invariants A_2 and A_3 are zero whereas near walls, A is close to zero because of the two component limit turbulence states. Moreover, a new term $(\Psi_{ij})^w_{sgs}$, inspired from the modelling of Gibson and Launder [20], is added in the original term Ψ_{ij} in order to account for the wall effects caused by the reflection of the pressure fluctuations from rigid walls

$$\begin{aligned}
(\Psi^w_{ij})_{sgs} &= c_{1w}\frac{\epsilon_{sgs}}{k_{sgs}}\left((\tau_{kl})_{sgs}n_k n_l\delta_{ij} - \tfrac{3}{2}(\tau_{ki})_{sgs}n_k n_j - \tfrac{3}{2}(\tau_{kj})_{sgs}n_k n_i\right) f_w \\
&+ c_{2w}\left((\Psi^2_{kl})_{sgs}n_k n_l\delta_{ij} - \tfrac{3}{2}(\Psi^2_{ik})_{sgs}n_k n_j - \tfrac{3}{2}\Psi^2_{jk}n_k n_i\right) f_w \qquad (49)
\end{aligned}$$

where in this expression, n_i is the unit vector perpendicular to the wall and f_w is a near wall damping function. Taking into account these developments, the modelled transport equation in a low Reynolds number version reads

$$\frac{D(\tau_{ij})_{sgs}}{Dt} = (P_{ij})_{sgs} + (\Psi^1_{ij})_{sgs} + (\Psi^2_{ij})_{sgs} + (\Psi^w_{ij})_{sgs} + (J_{ij})_{sgs} - \frac{2}{3}\epsilon_{sgs}\delta_{ij} \tag{50}$$

The dissipation rate ϵ_{sgs} equation (30) is also developed in a low Reynolds number formulation for approaching walls

$$\frac{D\epsilon_{sgs}}{Dt} = c_{sgs\epsilon_1}\frac{\epsilon_{sgs}}{k_{sgs}}P_{sgs} - c_{sgs\epsilon_2}\frac{\epsilon_{sgs}\tilde{\epsilon}_{sgs}}{k_{sgs}} + \frac{\partial}{\partial x_j}\left(\nu\frac{\partial\epsilon_{sgs}}{\partial x_j} + c_\epsilon\frac{k_{sgs}}{\epsilon_{sgs}}(\tau_{jm})_{sgs}\frac{\partial\epsilon_{sgs}}{\partial x_m}\right) \tag{51}$$

where $\tilde{\epsilon}_{sgs} = \epsilon_{sgs} - 2\nu(\partial\sqrt{k_{sgs}}/\partial x_n)^2$, x_n is the normal coordinate to the wall. The numerical constants of the model are the following $c_{sgs\epsilon_1} = c_{\epsilon_1} = 1.45$, $c_{\epsilon_2} = 1.9$, $c_{\epsilon_3} = 0.14$, $c_\epsilon = 0.18$. The functions used in equations (50) and (51) including $c_{sgs\epsilon_2}$ are listed in Table (1).

B Appendix: Realisability conditions

The question is to know if the subgrid stress model is able to satisfy the realisability conditions which imply non-negative values of the three principal invariants I_i appearing in the characteristic polynomial $P(\lambda) = \lambda^3 - I_1\lambda^2 + I_2\lambda - I_3$ deduced from the eigenvalue equation $|(\tau_{ij})_{sgs} - \lambda\delta_{ij}| = 0$ as mentioned by Schumann [43]. This question is crucial since a model which is not realisable cannot be retained for performing LES simulations. The expressions of the invariants I_i are the following

$$I_1 = (\tau_{ii})_{sgs} \geqslant 0 \tag{52}$$

$$I_2 = \frac{1}{2}[(\tau_{ii})_{sgs}(\tau_{jj})_{sgs} - (\tau_{ij})_{sgs}(\tau_{ji})_{sgs}] \geqslant 0 \tag{53}$$

$$I_3 = \frac{1}{6}[(\tau_{ii})_{sgs}(\tau_{jj})_{sgs}(\tau_{kk})_{sgs} - 3(\tau_{kk})_{sgs}(\tau_{ij})_{sgs}(\tau_{ji})_{sgs} + 2(\tau_{ij})_{sgs}(\tau_{jk})_{sgs}(\tau_{ki})_{sgs}] \geqslant 0 \tag{54}$$

where the usual Einstein summation convention is applied for the indices i, j, k. In practice, it is more convenient to analyse the weak form of the realisability conditions based on the transport equation (19) which require that when a principal subgrid-stress component vanishes, its time derivative must be positive to prevent negative values of the normal subgrid-stress components to appear [47]. From a physical standpoint, it is easier to examine the question of realisability in a coordinate system aligned with the principal axes of the subgrid stress tensor. By introducing the tensors p_{ij} and q_{ij} that allow to express the tensorial components $(\tau_{ij})_{sgs}$ from the local coordinate system to the principal coordinate system, the subgrid stress $(\tau^*_{ij})_{sgs}$ in the principal axes of coordinate is then computed by the tensorial relation

$$(\tau^*_{ij})_{sgs} = q_{il}\,(\tau_{lm})_{sgs}\,p_{mj} \tag{55}$$

verifying the property $p_{il}q_{lj} = \delta_{ij}$. The analysis is conducted in the particular case of homogeneous turbulence. Equation (19) is then considered and can be written in the compact form

$$\frac{\partial(\tau_{ij})_{sgs}}{\partial t} = (P_{ij})_{sgs} + (\Psi_{ij})_{sgs} - \frac{2}{3}\delta_{ij}\epsilon_{sgs} = S_{ij} \tag{56}$$

In this framework, the differentiation of equation (55) yields the resulting equation

$$\frac{\partial(\tau^*_{ij})_{sgs}}{\partial t} = \frac{\partial q_{il}}{\partial t} p_{lk}\,(\tau^*_{kj})_{sgs} + (\tau^*_{in})_{sgs}\,q_{nm}\frac{\partial p_{mj}}{\partial t} + q_{il}S_{lm}p_{mj} \tag{57}$$

Taking into account the derivative of the tensorial product $p_{il}q_{lj} = \delta_{ij}$

$$\frac{\partial(q_{il}\,p_{lj})}{\partial t} = \frac{\partial q_{il}}{\partial t}p_{lj} + q_{il}\frac{\partial p_{lj}}{\partial t} = 0\ , \tag{58}$$

it is a straightforward matter to show that equation (57) reduces to

$$\frac{\partial(\tau^*_{ij})_{sgs}}{\partial t} = \gamma_{ik}\,(\tau^*_{kj})_{sgs} - (\tau^*_{in})_{sgs}\,\gamma_{nj} + S^*_{ij} \tag{59}$$

where $\gamma_{ij} = q_{il}\,\partial p_{lj}/\partial t$ denotes a skew symmetric tensor. Therefore, equation (59) indicates that the turbulent subgrid stress $(\tau^*_{ii})_{sgs}$ can be written in the principal axes in the following way

$$\frac{\partial(\tau^*_{ii})_{sgs}}{\partial t} = (P^*_{ii})_{sgs} - c_{sgs_1}\frac{\epsilon_{sgs}}{k_{sgs}}\left((\tau_{ii})_{sgs} - \frac{2}{3}k_{sgs}\right) - c_2\left((P^*_{ii})_{sgs} - \frac{2}{3}P_{sgs}\right) - \frac{2}{3}\epsilon_{sgs} \tag{60}$$

where the Einstein summation convention is now suspended for indices ii. When the stress component $(\tau^*_{ii})_{sgs}$ vanishes, the production term in the principal axes $(P^*_{ii})_{sgs}$ goes also to zero so that the weak form of the realisability condition finally implies the relation

$$c_{sgs_1} \geqslant 1 - c_2\,\frac{P_{sgs}}{\epsilon_{sgs}} \tag{61}$$

For usual cases of flow physics, the production term of the turbulent energy is positive and therefore, due to the expression of the function c_{sgs_1} defined in equation (24) and table (1) for the model in its low Reynolds number version, the constraint equation (61) can be verified. The fact that the function c_{sgs_1}, depending on the parameter η, increases for large wave numbers enforces the realisability of the model. However, one can mention that the constraint (61) is not verified in all number of circumstances because the production incidentally can be negative. Note that for $i \neq j$, equation (59) becomes

$$\gamma_{ik}\,(\tau^*_{kj})_{sgs} - (\tau^*_{in})_{sgs}\,\gamma_{nj} + S^*_{ij} = 0 \tag{62}$$

allowing the determination of the tensor γ_{ik}.

C Appendix: Generation of isotropic turbulence in the spectral space with an imposed spectrum energy

The first step consists in generating an homogeneous isotropic field in a cubic box of size L using the method developed by Roy [36]. A random vector stream function in the spectral space is first defined

$$\hat{\psi}(\boldsymbol{\kappa}) = a(\boldsymbol{\kappa})\hat{\psi}_1(\boldsymbol{\kappa}) + jb(\boldsymbol{\kappa})\hat{\psi}_2(\boldsymbol{\kappa}) \tag{63}$$

where $\hat{\psi}_1$ and $\hat{\psi}_2$ are two vectors uniformly distributed on the sphere of radius unity in the half space $\kappa_3 > 0$. The stream function is computed in the half lower space $\kappa_3 < 0$ by the relation $\hat{\psi}(-\boldsymbol{\kappa}) = \hat{\psi}^*(\boldsymbol{\kappa})$, where $\hat{\psi}^*$ denotes the complex conjugate of $\hat{\psi}$, that ensure that velocity is in the real space. The fluctuating velocity is then obtained by the relation $\hat{u}_i = j\kappa_j\epsilon_{ijk}\hat{\psi}_k$. In order to obtain the given energy spectrum,

$$\langle \hat{u}_i(\boldsymbol{\kappa})\hat{u}_i(-\boldsymbol{\kappa})\rangle = \left(\frac{2\pi}{L}\right)^3 \frac{E(\kappa)}{2\pi\kappa^2} \tag{64}$$

the coefficients a and b appearing in equation (63) are then determined from the relations

$$a(\boldsymbol{\kappa}) = \frac{\cos(\lambda)}{||\epsilon_{ijk}\kappa_j\hat{\psi}_{1k}||}\left(\frac{2\pi}{L}\right)^{\frac{3}{2}}\left(\frac{E(\kappa)}{2\pi\kappa^2}\right)^{\frac{1}{2}} \tag{65}$$

$$b(\boldsymbol{\kappa}) = \frac{\sin(\lambda)}{||\epsilon_{ijk}\kappa_j\hat{\psi}_{2k}||}\left(\frac{2\pi}{L}\right)^{\frac{3}{2}}\left(\frac{E(\kappa)}{2\pi\kappa^2}\right)^{\frac{1}{2}} \tag{66}$$

where λ is a random number in the interval $[0, 2\pi]$. The velocity u in the physical space is then computed from its inverse Fourier transform

$$u_i(x_1, x_2, x_3) = \sum_{\kappa_1,\kappa_2,\kappa_3} \hat{u}_i(\kappa_1, \kappa_2, \kappa_3)\exp\left(j\kappa_m x_m\right) \tag{67}$$

References

[1] I. Befeno and R. Schiestel. Non-equilibrium mixing of turbulence scales using a continuous hybrid RANS/LES approach: Application to the shearless mixing layer. *Flow, Turbulence and Combustion*, 78:129–151, 2007.

[2] C. Cambon, D. Jeandel, and J. Mathieu. Spectral modelling of homogeneous non-isotropic turbulence. *Journal of Fluid Mechanics*, 104:247–262, 1981.

[3] B. Chaouat. Modélisation et simulation numériques d'écoulements de canal plan dans un repère fixe ou en rotation avec des modèles de turbulence du premier et du second ordre du type ASM et RSM. Technical report, ONERA, 1999. RTS 28/1145.

[4] B. Chaouat. Simulations of channel flows with effects of spanwise rotation or wall injection using a Reynolds stress model. *Journal of Fluid Engineering, ASME*, 123:2–10, 2001.

[5] B. Chaouat. Numerical predictions of channel flows with fluid injection using a Reynolds stress model. *Journal of Propulsion and Power*, 18(2):295–303, 2002.

[6] B. Chaouat. Reynolds stress transport modeling for high-lift airfoil flows. *AIAA Journal*, 44(10):2390–2403, 2006.

[7] B. Chaouat and R. Schiestel. Reynolds stress transport modelling for steady and unsteady channel flows with wall injection. *Journal of Turbulence*, 3:1–15, 2002.

[8] B. Chaouat and R. Schiestel. A new partially integrated transport model for subgrid-scale stresses and dissipation rate for turbulent developing flows. *Physics of Fluids*, 17(065106):1–19, 2005.

[9] B. Chaouat and R. Schiestel. From single-scale turbulence models to multiple-scale and subgrid-scale models by Fourier transform. *Theoretical Computational Fluid Dynamics*, 21(3):201–229, 2007.

[10] B. Chaouat and R. Schiestel. Hybrid RANS/LES modeling for non-equilibrium turbulent flows. *Proceeding of the* 5^{th} *Symposium on Turbulent Shear Flow Phenomena*, 2:753–758, 2007.

[11] G. Comte-Bellot and S. Corrsin. Simple Eulerian time correlation of full and narrow-band velocity signals in grid-generated, isotropic turbulence. *Journal of Fluid Mechanics*, 48:273–337, 1971.

[12] C. B. da Silva and J. C. F. Pereira. On the local equilibrium of the subgrid-scales: the velocity and scalar fields. *Physics of Fluids*, 108103:1–4, 2005.

[13] L. Davidson and M. Billson. Hybrid LES-RANS using synthesized turbulent fluctuations for forcing in the interface region. *International Journal of Heat and Fluid Flow*, 27:1028–1042, 2006.

[14] J. W. Deardorff. The use of subgrid transport equations in a three-dimensional model of atmospheric turbulence. *Journal of Fluid Engineering, ASME*, 95:429–438, 1973.

[15] A. Dejoan and R. Schiestel. LES of unsteady turbulence via a one-equation subgrid-scale transport model. *International Journal of Heat and Fluid Flow*, 23:398–412, 2002.

[16] J. Fröhlich, C. Mellen, W. Rodi, L. Temmerman, and M. Leschziner. Highly resolved large-eddy simulation of separated flow in a channel with streamwise periodic constriction. *Journal of Fluid Mechanics*, 526:19–66, 2005.

[17] T. B. Gatski, C. L. Rumsey, and R. Manceau. Current trends in modelling research for turbulent aerodynamic flows. *Phil. Trans. Royal Society*, 365:2389–2418, 2007.

[18] M. Germano. Turbulence: the filtering approach. *Journal of Fluid Mechanics*, 238:325–336, 1992.

[19] M. Germano, U. Piomelli, P. Moin, and W. H. Cabot. A dynamic subgrid-scale eddy-viscosity model. *Physics of Fluids*, 3(7):1760–1765, 1992.

[20] M. M. Gibson and B. E. Launder. Ground effects on pressure fluctuations in the atmospheric boundary layer. *Journal of Fluid Mechanics*, 86:491–511, 1978.

[21] S. S. Girimaji, E. Jeong, and R. Srinivasan. Partially averaged Navier-Stokes method for turbulence: Fixed point analysis and comparisons with unsteady partially averaged Navier-Stokes. *Journal of Applied Mechanics, ASME*, 73(3):422–429, 2006.

[22] F. Hamba. A hybrid RANS/LES simulation of turbulent channel flow. *Theoretical Computational Fluid Dynamics*, 16:387–403, 2003.

[23] K. Hanjalic, M. Hadziabdic, M. Temmerman, and M. Leschziner. Merging LES and RANS strategies: Zonal or seamless coupling ? In *Direct and Large eddy Simulations n° V*, pages 821–831. Ed. by R. Friedrich, B. Geurts and O. Métais, Kluwer Academic, May 2004.

[24] K. Hanjalic and S. Jakirlic. Contribution towards the second-moment closure modeling of separating turbulent flows. *Computers and Fluids*, 27(2):137–156, 1998.

[25] K. Horiuti and A. Yoshizawa. Large-eddy simulation of turbulent flow by 1-equation model. *Notes on Numerical Fluid Mechanics, Direct and large eddy simulations of turbulence, Vieweg Verlag*, 15:119–134, 1986.

[26] B. E. Launder and N. Shima. Second moment closure for the near wall sublayer: Development and application. *AIAA Journal*, 27(10):1319–1325, 1989.

[27] M. A. Leschziner and D. Drikakis. Turbulence modelling and turbulent-flow computation in aeronautics. *The Aeronautical Journal*, 106:349–384, 2002.

[28] M. Lesieur and O. Metais. New trends in large-eddy simulations of turbulence. *Ann. Rev Journal of Fluid Mechanics*, 28:45–82, 1996.

[29] D. K. Lilly. Numerical simulations of developing and decaying two-dimensional turbulence. *Journal of Fluid Mechanics*, 45:395–415, 1971.

[30] J. L. Lumley. Computational modeling of turbulent flows. *Advances in Applied Mechanics*, 18:123–176, 1978.

[31] P. Mellen, J. Fröhlich, and W. Rodi. Lessons from lesfoil project on large-eddy simulation of flow around an airfoil. *AIAA Journal*, 41(4):573–581, 2003.

[32] O. Métais and M. Lesieur. Spectral large-eddy simulation of isotropic and stably stratified turbulence. *Journal of Fluid Mechanics*, 239:157–194, 1992.

[33] P. Moin and J. Kim. Numerical investigation of turbulent channel flow. *Journal of Fluid Mechanics*, 118:341–377, 1982.

[34] R. Moser, D. Kim, and N. Mansour. Direct numerical simulation of turbulent channel flow up to $R_\tau = 590$. *Physics of Fluids*, 11(4):943–945, 1999.

[35] R. S. Rogallo. Numerical experiments in homogeneous turbulence. In *Proc. Conf. on Computational of Complex Turbulent Flows, Stanford Univ. Calif.*, 1981.

[36] P. Roy. Résolution des équations de Navier-Stokes par un schéma de haute précision en espace et en temps. *La Recherche Aérospatiale*, 6:373–385, 1980.

[37] C. L. Rumsey and T. B. Gatski. Recent turbulence model advances applied to multielement airfoil computations. *Journal of Aircraft*, 38(5):904–910, 2001.

[38] R. Schiestel. Multiple-time scale modeling of turbulent flows in one point closures. *Physics of Fluids*, 30(3):722–731, 1987.

[39] R. Schiestel. Study of one-dimensional spectral dynamic equations of the Reynolds stresses in homogeneous anisotropic turbulence: Application to split-spectrum modelinge. In *Proc. of the Summer Program, Center for Turbulence Research, Stanford Univ. Calif.*, pages 95–108, 1987.

[40] R. Schiestel. *Modeling and simulation of turbulent flows.* ISTE Ltd and J. Wiley, 2008.

[41] R. Schiestel and B. Chaouat. On partially integrated transport models for subgrid-scale modelling. *ERCOFTAC Bulletin*, 72:49–54, 2007.

[42] R. Schiestel and A. Dejoan. Towards a new partially integrated transport model for coarse grid and unsteady turbulent flow simulations. *Theoretical Computational Fluid Dynamics*, 18:443–468, 2005.

[43] U. Schumann. Realizability of Reynolds stress turbulence models. *Physics of Fluids*, 20(5):721–725, 1977.

[44] A. Scotti, C. Meneveau, and D. K. Lilly. Generalized smagorinsky model for anisotropic grids. *Physics of Fluids*, 5(9), 1993.

[45] P. R. Spalart. Strategies for turbulence modelling and simulations. *International Journal of Heat and Fluid Flow*, 21:252–263, 2000.

[46] P. R. Spalart and S. R. Allmaras. A one-equation turbulence model for aerodynamic flows. *La Recherche Aérospatiale*, 1:5–21, 1994.

[47] C. G. Speziale, R. Abid, and P. A. Durbin. On the realisability of Reynolds stress turbulence closures. *Journal of Scientific Computing*, 9(4):369–403, 1994.

[48] C. G. Speziale, S. Sarkar, and T. B. Gatski. Modelling the pressure-strain correlation of turbulence: an invariant dynamical systems approach. *Journal of Fluid Mechanics*, 227:245–272, 1991.

[49] L. Temmerman, M. Hadziabdic, M. A. Leschziner, and K. Hanjalic. A hybrid two-layer URANS-LES approach for large eddy simulation at high Reynolds numbers. *International Journal of Heat and Fluid Flow*, 26:173–190, 2005.

[50] F. Tessicini and M. A. Leschziner. Large eddy simulation of three-dimensional flow around a hill-shaped obstruction with a zonal near-wall approximation. *International Journal of Heat and Fluid Flow*, 27:894–908, 2007.